

https://dspace.org/

Multigeophysical methods for characterizing fractures in an open pit mine western Bushveld Complex South Africa

Moyagabo Rapetsoa; Sikelela Gomo; Musa Manzi; Ian James; Jureya Dildar ...

WILEY-BLACKWELL
https://hdl.handle.net/10539/40690
WOS

Downloaded from a DSpace repository. https://dspace.org/

Check for updates

Received: 19 December 2022 | Accepted: 1 February 2024

DOI: 10.1111/1365-2478.13489

Geophysical Prospecting | EAGE EUROPEAN ASSOCIATION OF GEOSCIENTISTS & ENGINEERS

ORIGINAL ARTICLE

Multi-geophysical methods for characterizing fractures in an open pit mine, western Bushveld Complex, South Africa

Moyagabo K. Rapetsoa[1] | **Sikelela Gomo**[1] | **Musa S. D. Manzi**[1] | **Ian James**[1,2] | **Jureya Dildar**[1] | **Mpofana Sihoyiya**[1] | **Ndamulelo Mutshafa**[1] | **Raymond J. Durrheim**[1]

[1]School of Geosciences, University of the Witwatersrand, Johannesburg, Republic of South Africa

[2]Southern Geoscience Consultants, West Perth, Western Australia, Australia

Correspondence
Moyagabo K. Rapetsoa, School of Geosciences, University of the Witwatersrand, Private Bag, Wits, Johannesburg 2050, Republic of South Africa. Email: 867109@students.wits.ac.za

Funding information
National Research Foundation (NRF); Centre of Excellence for Integrated Mineral and Energy Resource Analysis (DSI-NRF Cimera), Grant/Award Number: 91487

Abstract

In the Bushveld Complex, South Africa, open pit mines are faced with a challenge of rock slope stability due to geological structures (fractures, faults and dykes) that compartmentalize the rock mass. Geophysical surveys (seismics, magnetics and electrical methods) were conducted in a 0.2 km^2 area at Tharisa mine, with the goal to delineate fractures that may be potential conduits for water migration into the pit. Special processing techniques were applied to the dataset to obtain good quality seismic, magnetic and resistivity models. The P-wave velocity models show distinct low velocities in the centre of the seismic profile, indicating the presence of weak zones associated with faulting or fracturing. Seismic reflection method was used to image the deeper discontinuities and mineralization contacts. Near surface reflections are observed throughout the profiles and are correlated with the contact between the chromitite and host rock. Ground magnetic surveys were conducted to delineate dykes and fractures. De-trending and de-culturing techniques were applied on the magnetic data for correcting regional and temporal variations. The low magnetic regions indicate the presence of fracture systems in the subsurface, whereas the high magnetic region is correlated with the dolerite dyke that crosscuts the pit. The electrical resistivity tomography exhibits linear low resistivity contrast zones that differentiate between the fractured and undisturbed hard rock at an estimated depth of 4–10 m. Resistivity shows discontinuities that suggests the presence of fracturing and dyke-host rock contacts. Correlation among magnetics, P-wave velocity models, resistivity section and seismic data is evident when overlaying the different datasets, implying that the low magnetic regions are highly weathered and prone to fracturing. The integration of geophysical data is encouraging, because it was able to image the depth to the bedrock, fractures within the host rock and dyke in a complex mining environment.

KEYWORDS
fractures, groundwater, imaging, interpretation, hydromigration

This is an open access article under the terms of the Creative Commons Attribution-NonCommercial License, which permits use, distribution and reproduction in any medium, provided the original work is properly cited and is not used for commercial purposes.
© 2024 The Authors. *Geophysical Prospecting* published by John Wiley & Sons Ltd on behalf of European Association of Geoscientists & Engineers.

INTRODUCTION

Tharisa mine is an open pit (Figure 1a) mine located in the North-west province of South Africa, 35 km east of Rustenburg. The mine is located in a hard rock environment within the Bushveld Complex (BC). The BC exhibits joints of tectonic origin, with varying orientation (planar and non-planar) and intensity across the BC. Joints are often coupled with other geological structures such as dykes, veins and faults (Figure 1b). Systematic joints (planar) are a set of parallel joints spaced evenly apart (Perritt & Roberts, 2007; Roberts & Clark-Mostert, 2010). Majority of the joints in the study area are sub-vertical and can be divided into two sets (Figure 1c), parallel sets (cyan, green and blue) and perpendicular sets (pink, yellow and red) to a fault zones that cross cut the pit and parallel to a dyke (Figure 1b). Non-systematic joints occur randomly in the study area due to mine blast stress regime. The sub-vertical joints intersect the sub-horizontal interlayering planes of the middle group chromitites.

Most open pit mines are faced with a challenge of rock slope stability due to geological structures that cause discontinuities of the rock mass. The fractures introduce mining, engineering and hydrogeological challenges. The development of the mine promotes the increase in fractures through blasting and excavation of the bedrock. Fractures may act as conduits for migration of groundwater (e.g. water from rivers and aquifers) into the pit, which floods the pit and causes delays in production (Ofterdinger et al., 2019; Titus et al., 2009).

Near-surface geophysical methods have grown widely in addressing mining, engineering and environmental problems, for example mineral exploration, detection of buried pipes, sinkholes and fracture mapping (Amoush & Mashagbeh, 2009; Dahlin, 1996; Kerrigan, 2013; Pazzi et al., 2018; Van Schoor, 2002). The need to delineate the fractures and understand the migration of water into the mine pit has led to the development of multi-geophysical and hydrological acquisition setups for gathering data in the noisy mine environments. The main objectives of this study are as follows: (1) to use geophysical methods to locate and characterize fractures in an open pit mine, (2) to understand the ground water migration into the pit and associate it with the geological structures

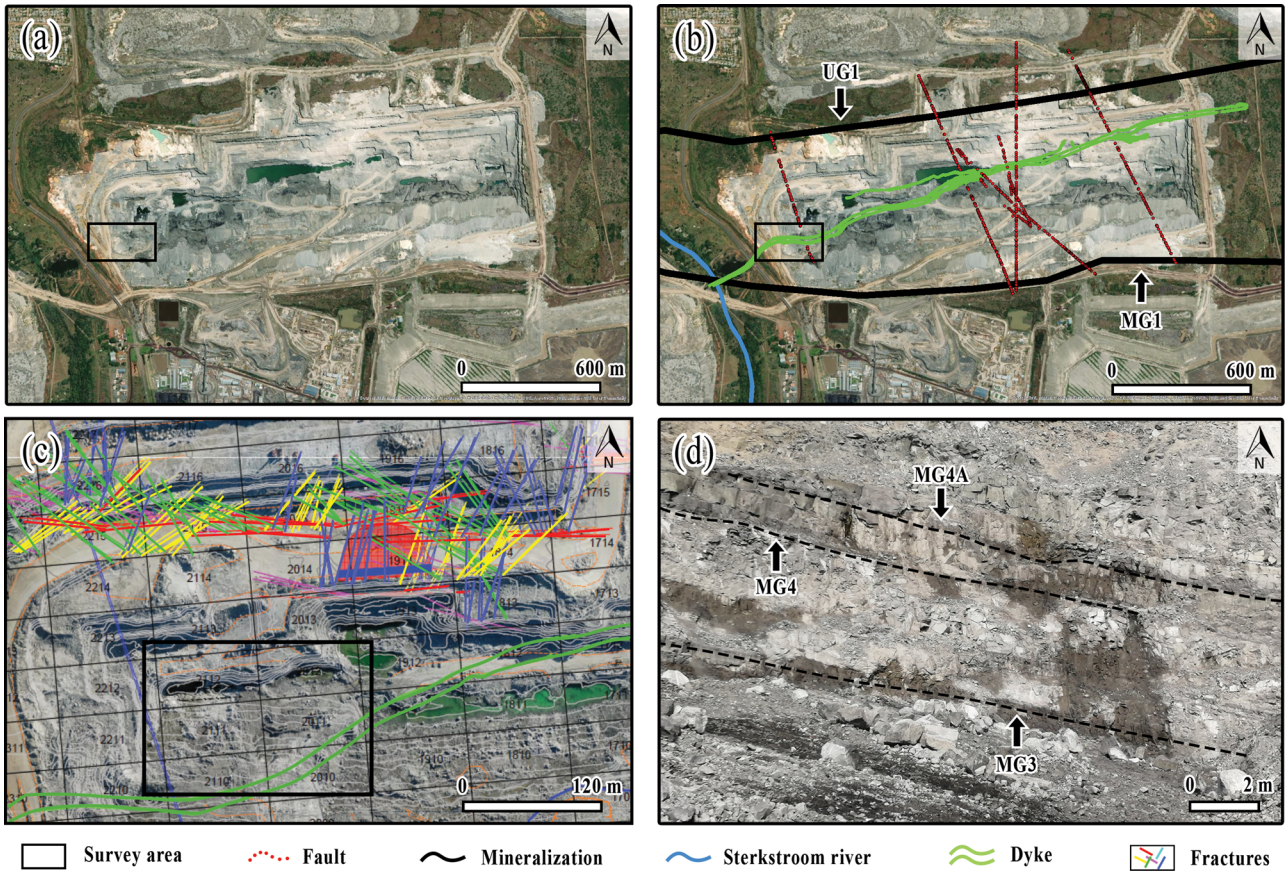

FIGURE 1 (a) Aerial photo of Tharisa mine east pit. (b) Major dyke (green) and faults (red) cross-cutting the west pit at Tharisa mine. Sterkstroom River (blue) divides the mine into a west pit and an east pit. The mineralization (black: UG1 and MG1) runs parallel to the ends of the east pit (c) Mapped fractures (red, blue, green, pink, yellow and cyan) at the Tharisa mine with varying orientations. (d) Sidewall, showing inter-bedding and cross-cutting joints. Dark areas are areas where water is seeping into the pit.

13652478, 2024, 5, Downloaded from https://onlinelibrary.wiley.com/doi/10.1111/1365-2478.13489 by South African Medical Research, Wiley Online Library on [21/05/2024]. See the Terms and Conditions (https://onlinelibrary.wiley.com/terms-and-conditions) on Wiley Online Library for rules of use; OA articles are governed by the applicable Creative Commons License

around the pit, (3) to delineate the depth of the mineralization and its associated geological structures beyond the mined out areas and (4) to address challenges encountered in geological complex and mine noisy environment when acquiring geophysical data.

The use of multi-geophysical methods (seismics refraction [SRT] and reflection, magnetics and electrical resistivity tomography [ERT]) to image structures depends on multiple factors such as the survey design (receiver and source positions), physical properties of the host rock, geometry (e.g. size and depth), structural characteristics of the target and the mine noise levels. In this study, we also demonstrate the challenges faced by the geophysical methods (i.e. magnetics, SRT and ERT) to characterize near-surface fractures and mineralization in a mining area with large infrastructure, trucks and electrical powerlines that cause interfering noise during acquisition. This study forms part two of the three part integrated geophysical, hydrogeology and geochemical studies to further unravel and determine the source of water that migrates into the pit. Gomo et al. (2023) presented an integrated geophysical approach to delineate boulders in an active open pit mine as part I. Part III of the study (Dildar et al., 2023) focused on integration of the hydrogeology and geochemical data with near surface geophysical methods.

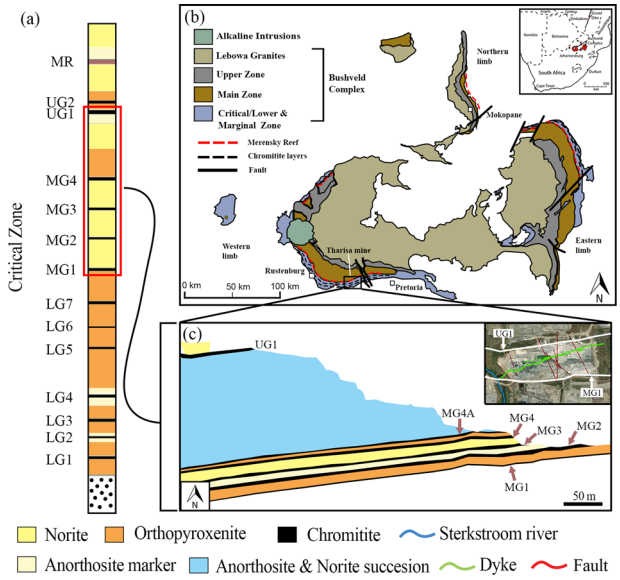

FIGURE 2 (a) Stratigraphic column of the critical zone, highlighting the chromitite layers that are exploited at the Tharisa mine. (b) General geological map of the Bushveld complex showing major faults, economical horizons, and the location of the study area. (c) Simplified geology of the Tharisa mine, with an insert showing the location of the far end mineralizations (white: MG1 and UG1) that are being exploited at the mine, together with geological structures and a river that crosscut the east pit.

GEOLOGICAL SETTING AND THARISA MINE

The Bushveld Complex (BC) covers an area of about 65,000 km^2 (Figure 2), typified by a shape of a broad oval, with a long extension of 375 km east–west and 300 km wide to the north–south. The BC is the largest mafic-ultramafic layered igneous intrusion, divided into five limbs that are emplaced on the Transvaal Supergroup at 2058.9 ± 0.8 Ma, with a thickness of 9 km. The geology and stratigraphy of the BC (Figure 2a,b) is well documented by several authors (e.g. Basson, 2019; Cawthorn, 2015; Eales & Cawthorn, 1996; Kinnaird, 2005; Wilson, 2005).

The mineralization at Tharisa mine is situated in the critical zone (CZ) of the BC. The mine is split into two pits (east and west pits) by the Sterkstroom River (Figure 1b) and exploits the Middle Group (MG) chromitites (Figure 2c: MG4, MG3, MG2 and MG1), with the UG1 being 165–18 m above the MG. Mining of UG1 happened in the past, with the shallow MG1 being mined underground. The mine plans on having underground operations in the future to exploit the deeper MG2 and MG4 mineralizations. The CZ is made up of pyroxenites, anorthosites, norites and stringers of chromitite. The general dip of the mineralization is between 9° and 15° to the north, with the thickness of the MGs and UG1 ranging from few centimetres to 3 m. The geological structures of the Tharisa mine region have been interpreted using aeromagnetic, drilling data and open pit observations (Lotheringen et al., 2016). An approximately 15 m thick, NE–SW trending and near-vertical dyke that crosscuts the west pit is the most dominant feature mapped by the aeromagnetic data (Figure 1b). Multiple faults are mapped within the pit and crosscut the pit with a predominant strike of NNW–SSE, which coincides with the planes of weaknesses that reactivated during the emplacement of the BC. The fractures in the BC are known to be associated with dykes and faults (Bumby et al., 2012; Hartzenberg & Plessis, 2014). The fracturing is observed on the northern part of the pit and our study focuses on characterizing the fractures on the southern part of the pit.

GEOPHYSICAL DATA

In this section, we summarize the physical properties, acquisition and processing of the seismic, magnetics and resistivity data that were collected at Tharisa mine.

Physical properties

To complement the geophysical data, rock samples and borehole data were collected from the Tharisa mine. To the best of our knowledge, the borehole data only include the geological

13652478, 2024, 5, Downloaded from https://onlinelibrary.wiley.com/doi/10.1111/1365-2478.13489 by South African Medical Research, Wiley Online Library on [21/05/2024]. See the Terms and Conditions (https://onlinelibrary.wiley.com/terms-and-conditions) on Wiley Online Library for rules of use; OA articles are governed by the applicable Creative Commons License

logging. There is no downhole petro-physical data available for the study site. To complement the borehole data, we have gathered more petro-physical data from the Council of Geosciences database and measurements from Sepato (2015). The data used from the above mentioned database were filtered to boreholes that are closer to Tharisa mine. The laboratory measurements in this study were P-wave velocity, bulk density and magnetic susceptibility measurements, whereas resistivity measurements were sourced from the literature (Maré, 2022). The samples were norites, anorthosites, chromitite and pyroxenites, and the resistivity measurements for pyroxenite were not found in the literature. The collected samples were prepared for bulk density, P-wave velocity and magnetic susceptibility measurements at room temperature and pressure using ultrasonic frequencies. The ideal conditions to measure the samples are under elevated stress (~20–60 MPa) to mimic the in situ environments, but due to a lack of equipment in our laboratory, the measurements were not done at elevated temperature and stress. A high frequency signal is produced by the transducers and passes through the rock sample. The signal is observed through the oscilloscope and the waveform is recorded by the computer. P-wave velocities are estimated from the measured travel times of the high frequency acoustic pulses through the samples. Bulk densities were collected using the immersion techniques, were sampled and were suspended in pure water, and the density of the sample was estimated by the use of the Archimedes principle.

Data acquisition

Prior to data acquisition, appropriate acquisition parameters need to be assessed, together with the expected response of the target through forward modelling. Forward modelling can also assist in validating the interpretation of the dataset and provide information for mineral exploration and risk assessment (Malehmir et al., 2013; Manzi et al., 2017; Maries et al., 2020; Rapetsoa et al., 2022).

Seismics

The seismic data for this study were collected in October 2021. Two seismic profiles were collected with a total length of 150 m: One of the seismic profiles (SP1 96 m long) was inside the pit, whereas SP2 (46 m) was collected at the edge of the pit. As the study area is inside the pit, where certain areas are hard rock, a combination of different geophone setup was used. A land streamer (4.5 Hz) and spiked geophones (14 Hz) were used along SP1 (Figure 3a,b), with a receiver spacing of 2 m. For SP2, 14 Hz 1C spiked geophones were used, with a receiver spacing of 1 m (Table 1). The seismic profiles (Figure 4a) were setup to be perpendicular to the faults and fractures systems observed on the aeromagnetic data in and around the pit, with the main dyke being parallel to the lines (Figure 4a). For safety reasons, source and receiver positions were limited by the active mine roads; therefore, the length of some of the seismic profiles were shorter than desired. Although multiple profiles were collected (named SP1–SP8), this study focuses on the data obtained from SP1 and SP2 due to their location and essential for studying the fracture system of the east pit.

Prior to collecting the data, we first performed a test to compare the seismic sources (6.3 kg sledgehammer and a 24 kg accelerated weight drop [AWD]). From the test, it was evident that the sledgehammer was suitable for this study, as it preserved the near-offset traces, whereas the AWD over drives the near-offset geophones by having powerful source impulse. The sledgehammer was also chosen for its applicability in uneven terrains. Noise conditions were different from profile to profile. When acquiring the data in the open pit, there was drilling, dump trucks and loader (Figure 3c) working near the profile. We did not have permission to acquire seismic data during night time; therefore, all our seismic profiles were collected during working hours (08:00 and 17:00) where the mining activity and traffic from the main road were high. The receiver and shot positions (eastings, northings and elevation) were surveyed using a real time Differential Global Positioning System device. The shots were recorded at every 2 m for SP1 and 1 m for SP2, and four shot records were acquired at every shot position using the sledge hammer and vertically stacked to increase the signal-to-noise ratio (SNR). We analysed and tested different sampling rates, with SP2 being recorded first with a sampling rate of 0.25 ms, whereas SP1 was recorded with a sampling rate of 1 ms. A sampling rate of 1 ms was chosen for the rest of the seismic profiles, as it provided better results with respect to the high frequencies and spurious frequencies. A total of 96 shots and 4608 traces were generated after vertically stacking the repeated shots.

Magnetics

A three phased 5-day field survey in 2021 was conducted to collect total magnetic field data at Tharisa mine. The survey started with an assessment of the pit to locate mine benches that have seepage of water and a dyke, which are a guide to the location of fractures (Figure 1d). The magnetic survey covered a total area of 16,300 m^2 using two G856 proton precession magnetometers and a G859 cesium vapour magnetometer. The G856 magnetometers were used as base stations and placed at two different locations (with no cultural noise), mounted on a 2.5 m vertical aluminium pole. The magnetometers (G856) were set to record stationary readings at every 30 s interval, and the data were then inspected and compared

13652478, 2024, 5, Downloaded from https://onlinelibrary.wiley.com/doi/10.1111/1365-2478.13489 by South African Medical Research, Wiley Online Library on [21/05/2024]. See the Terms and Conditions (https://onlinelibrary.wiley.com/terms-and-conditions) on Wiley Online Library for rules of use; OA articles are governed by the applicable Creative Commons License

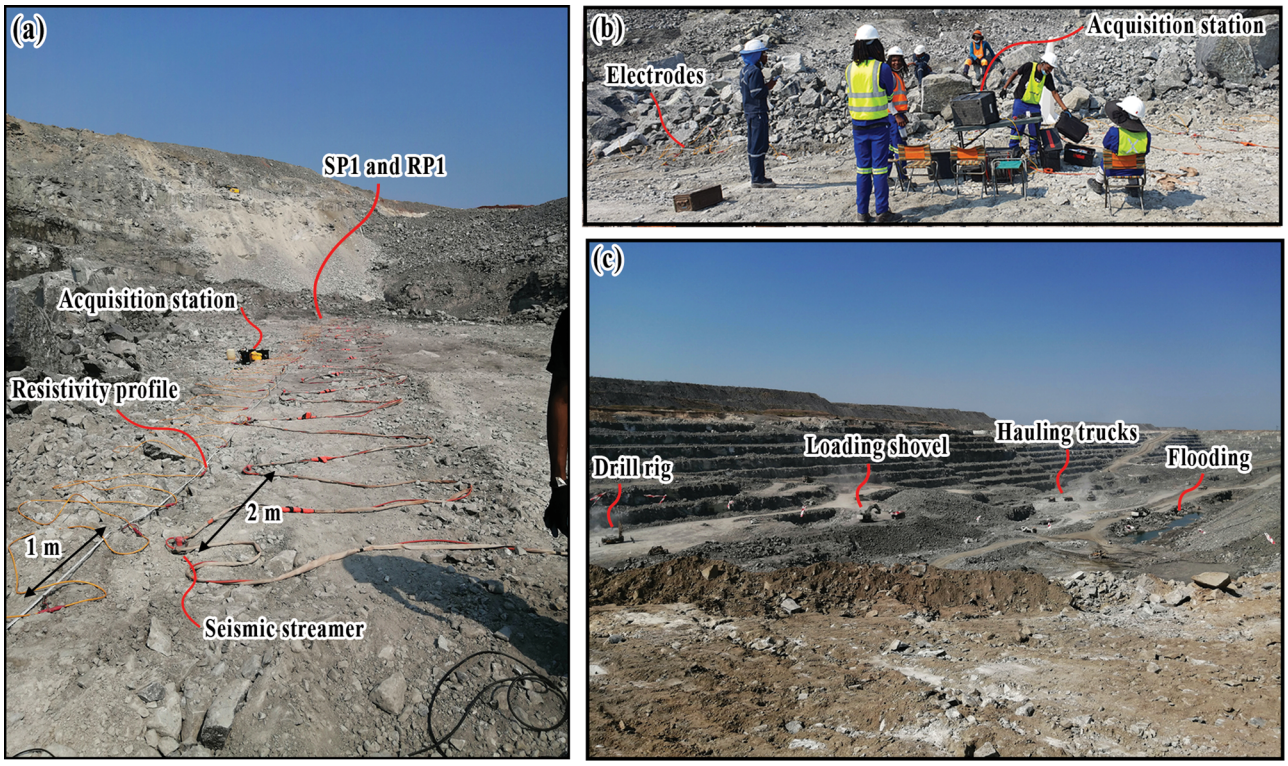

FIGURE 3 (a and b) Field photo showing the acquisition setup for seismic and resistivity profiles inside the pit using a seismic land streamer. (c) Field conditions during data acquisition at Tharisa mine, with mining activity near seismic profile.

TABLE 1 Main reflection seismic data acquisition parameters.

Profiles	**SP1**	**SP2**
Survey parameters		
Acquisition type	Fixed straight line	Fixed straight line
Acquisition system	Geometric Geode	Geometric Geode
Receiver frequency (Hz)	04.5 and 14	14
Type of base	land streamer and 7 cm spike	7 cm spike
No. of receivers	48	48
Receiver spacing	2	1 m
Source	6.3 kg sledgehammer	6.3 kg sledgehammer
Source spacing (m)	2	1
Profile length (m)	96	50
Recording length (ms)	1000	500
Sampling interval (ms)	1	0.25

for spikes in the diurnal curve. The G895 magnetometer was used as a rover for acquisition of the magnetic profiles. The GPS antenna was vertically mounted ~3 m, and the magnetic sensor was mounted ~2 m. The three grids (Figure 4b) were surveyed in a fast 'walking mode', with the rover magnetometer (G859) carried on a non-magnetic backpack along the profiles. The operator was walking at an approximate speed of 1 m/s on open land, with a sampling rate of 1 s. Although certain sections in the pit required a reduction of speed due to deep excavations. The walking mode GPS positioning error is ±1 m. A section of the dyke (Figure 4b: MS1) was surveyed in great detail with nine parallel N–E ground magnetic lines of 70 m in length, with a line spacing of 10 m. Grids 2 and 3 had magnetic lines of over an area of 20–70 m × 10–70 m and 40 × 70 m^2. Regional aeromagnetic data (Figure 4c) were used to identify major structures such as dykes and faults. The dyke crosses the pit (Figure 1b), covers a full length of 2.91 km and has thickness between 10 and 15 m.

13652478, 2024, 5, Downloaded from https://onlinelibrary.wiley.com/doi/10.1111/1365-2478.13489 by South African Medical Research, Wiley Online Library on [21/05/2024]. See the Terms and Conditions (https://onlinelibrary.wiley.com/terms-and-conditions) on Wiley Online Library for rules of use; OA articles are governed by the applicable Creative Commons License

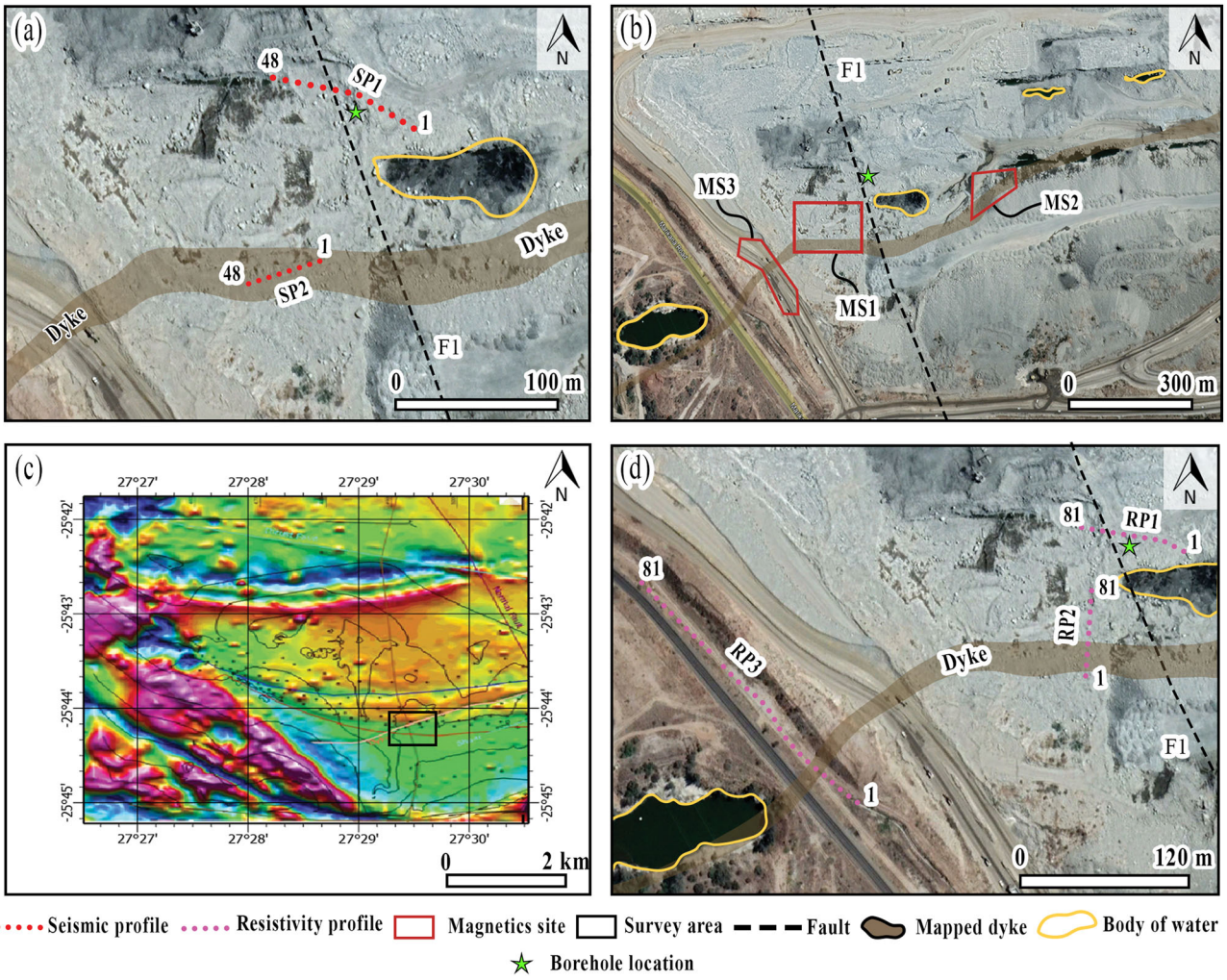

FIGURE 4 Aerial photos showing the location of two major geological structures (fault and dyke) and (a) seismic profiles (two seismic profiles inside the pit, with a combination of different sensors), (b) magnetic grids (over the geological structures), (c) Regional aeromagnetic data over the edge of the western Bushveld complex, showing major geological structures and site location and, (d) resistivity profiles. MS, magnetic site; RP, resistivity profile; SP, seismic profile.

Resistivity

The electrical resistivity surveys were conducted in two phases. The first phase was for testing the method for imaging and characterizing the chromitite orebody prior to drilling. The second phase was the application of resistivity to locate geological structures (faults, fractures and dykes) that may act as conduit for water migration into the pit.

The first phase involved one profile (Figure 4d: RP1) that was located in the pit over known mineralization, with a strike of E–W. The profile was surveyed using the ABEM Terrameter SAS 1200, with 41 fixed electrodes that are spaced 2 m apart in a Schlumberger, Wenner and dipole–dipole array (Reynolds, 2011). All the electrodes (Figure 3a,b) were hammered at least 20 cm into the ground to ensure good coupling. The input current was set to 10 mA and the contact resistance was of the order 200–3000 Ω. The system automatically reports any anomalous contact resistance (negative resistivity readings), and a solution to this was re-planting the electrode or watering the electrode point. The second phase comprised two resistivity profiles (Figure 4d) with length of 80 m for RP2 and 240 m for RP3. The first profile (RP2), striking S–N, was conducted at the edge of the pit with the aim of imaging the structures that cause seepage (Figure 1d) into the pit. The survey was conducted over an area with fractured rock and a little topographic variation (<1 m). Forty-one fixed electrodes were used for each of the two profiles, with a spacing of 2 m for RP2 and 6 m for RP3. RP2 was perpendicular to the strike of the mineralization, and the length was limited by trenches. RP3, on the other hand, had a strike of SE-NW and was designed to delineate water conduits that might be transporting water from the river to the west of the pit. The profile was acquired

13652478, 2024, 5, Downloaded from https://onlinelibrary.wiley.com/doi/10.1111/1365-2478.13489 by South African Medical Research, Wiley Online Library on [21/05/2024]. See the Terms and Conditions (https://onlinelibrary.wiley.com/terms-and-conditions) on Wiley Online Library for rules of use; OA articles are governed by the applicable Creative Commons License

over an area covered with loose sandy soil, located parallel to the road in the west of the east pit (Figure 4d).

Data Processing

Seismics imaging

The collected seismic profiles were designed to cover the east pit of Tharisa mine, particularly the edge of the pit, where the mapped fractures (Figure 1c) are dominant, and there is evidence of water flow on the benches (Figure 1d). The profiles were collected on clear tracks and inside the pit for effective shot positions. This resulted in the introduction of noise due to the proximity of the roads and mine workings. Figure 5 shows raw shot gathers and processed shot gathers. The raw shot gathers (Figure 5a,b) were noisy on the far offsets due to, for example, vibrations generated by drilling (Figure 5a: marked with green arrow), and some shots exhibit events that come in later that are due to secondary sources (e.g. dump trucks and loaders).

However, majority of the shots have good SNR (e.g. SP2) and show strong shallow P-wave reflections. Processing of the seismic data involved the suppression of the noise to further enhance the P-wave reflections that are caused by lithological boundaries. Reflections are observed in the shallow subsurface between 0 and 100 ms (Figure 5c,d). Data processing flow (Figure 6) started with fixing and adding the geometry for all the seismic profiles, and assigning the common depth points spacing of 1 m for SP1 and 0.5 m for SP2. Approximately 2358 first breaks were carefully picked (manual) on each profile for refraction statics and to generate a two layered P-wave velocity model. The refraction statics improved the continuity of the first arrivals and enhanced the reflections. A constant replacement velocity of 5000 m/s was chosen together with a matching datum of 1109 and 1142 m for SP1 and SP2, respectively. Spectral analysis of the seismic profiles shows that the data have frequency range of 0–500 Hz for SP1, whereas SP2 has a frequency range of 0–2000 Hz due to the sampling rate during acquisition. The source energy frequency of the seismic data was in the range of 35–125 Hz; therefore, we applied band pass filter of 30–45–180–200 Hz. The filter was designed to attenuate the high frequency noise (>300 Hz) introduced during acquisition and also to reduce the low-frequency noise from the ground roll and random noise generated by mine workings. We applied f-k filter on the data to remove the steeply dipping air waves and guided waves. The effect of f-k filter is clearly demonstrated on SP2 by attenuating the steeply dipping secondary source energy (Figure 5b). A gapped deconvolution with a gap length of 6 ms was applied to broaden the frequency spectrum and reduce source signal. The pre-stack processing flow enhanced the subsurface reflections as shown in Figure 5c,d. Prior to normal moveout (NMO) corrections (60% stretch mute), we applied first break mutes to kill the high amplitude first breaks, such that they do not affect the final stack section and enhance near surface reflections.

A series of constant velocities were tested ranging from 1500 to 5000 m/s with 250 m/s intervals. Through visual inspection, an estimate NMO velocity of 3000 m/s was used for SP1 and 2500 m/s for SP2 for stacking. Post-stack filtering involved fx-deconvolution, spectral weighting and semblance to enhance the continuity of the reflections and improve the final image. We compared the phase shift and Kirchoff migration methods, and the Kirchhoff migration with constant velocity of 3000 m/s produced the best image. The seismic data were depth converted using 3000 m/s for final interpretation.

2D travel time tomography

The target fractures within the subsurface can be imaged using seismic tomography. First break picking was conducted with an average of 2358 picks on each profile. A quality check was conducted, and bad quality picks were removed prior to the inversion. Following picking of the data, an initial model was created. A non-linear, first-arrival travel time tomographic inversion with Tikhonov regularisation (Zhang & Toksöz, 1998) was run until convergence was achieved. This processes the ray trace synthetic travel times for each shot such that the difference between the input and synthetic first break picks are minimized. Initial analysis of the model was conducted, checking the model misfit on a shot-by-shot and receiver-by-receiver basis. Where a significant misfit was present, the first break picks were checked for consistency. Subsequently, the data quality was checked, and, provided there was an acceptable convergence, the tomograms were exported and integrated in the interpretation (James et al., 2019). The final models for SP1 and SP2 had root mean square (RMS) of about 4 and 2 ms after 5 and 10 iterations, respectively. The quality of picks was reasonable considering the noisy environment. The velocities ranging from 500 m/s (loose rocks) to 6500 m/s (bedrock) were considered reasonable for the final model of the two profiles. Refracted arrivals are noticeable in both SP1 and SP2 when inspecting the first arrival versus offset (Figure 7a,b) used for the tomography. Travel time residuals are shown in Figure 7c,d as a function of offset for both profiles. As a result of the near surface velocity region and maximum offsets between 50 and 100 m, a maximum ray penetration of 16–24 m is observed in the velocity models.

Magnetics

The magnetic data were dumped and corrected for diurnal (temporal) variations. The processing of the data involved the

13652478, 2024, 5, Downloaded from https://onlinelibrary.wiley.com/doi/10.1111/1365-2478.13489 by South African Medical Research, Wiley Online Library on [21/05/2024]. See the Terms and Conditions (https://onlinelibrary.wiley.com/terms-and-conditions) on Wiley Online Library for rules of use; OA articles are governed by the applicable Creative Commons License

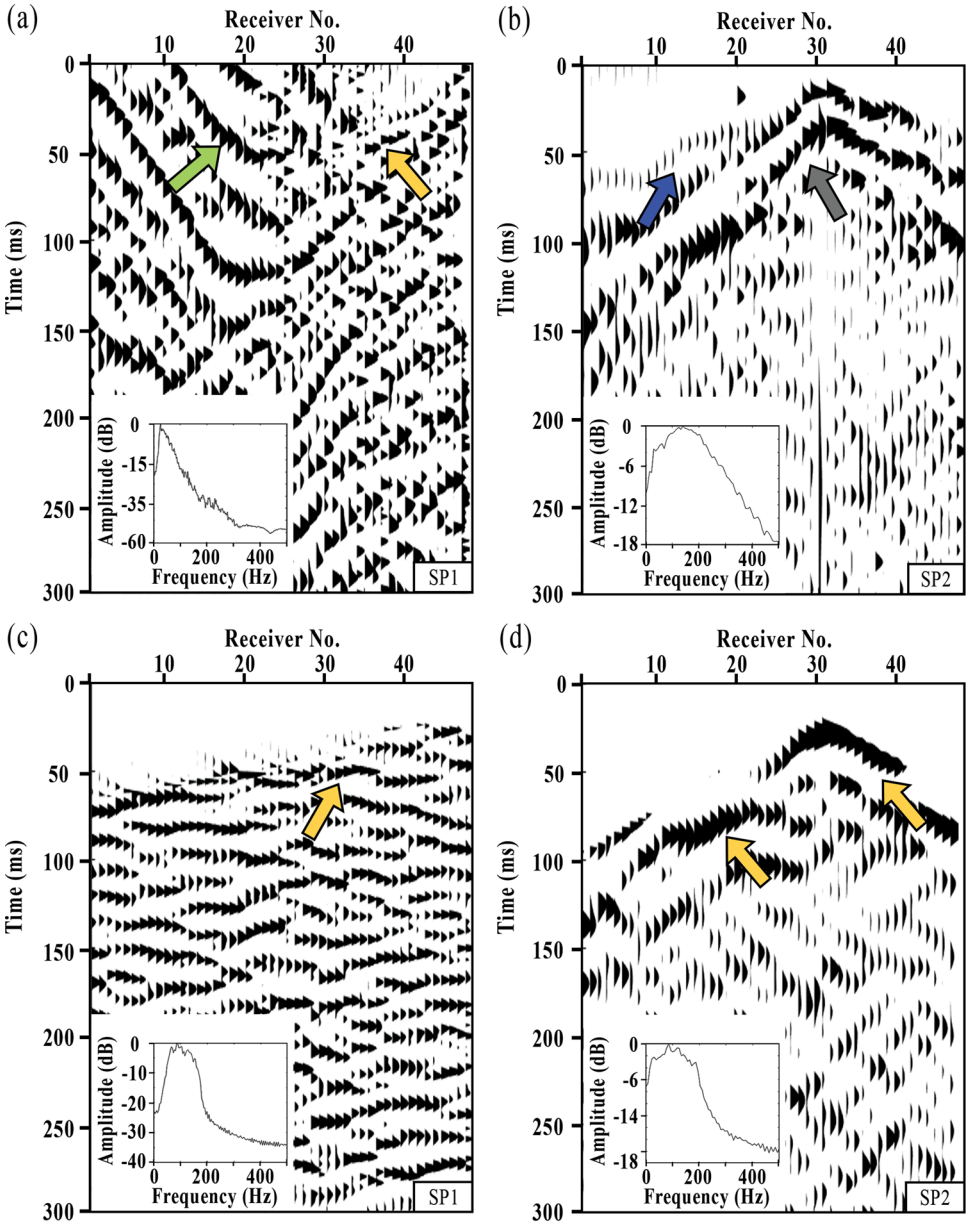

FIGURE 5 (a and b) An example of a raw shot gathers from the two seismic profiles (SP1 and SP2), showing the quality of the data inside the open pit, with clear first breaks (blue arrow) on SP2. The green arrow shows noise generated by mine workings. Inserts show amplitude spectra; (c and d) processed shot gathers. The yellow arrows show some reflections recorded in the shot gather, whereas the grey arrow indicates the surface and guided waves.

removal of the regional magnetic field (de-trending), manual de-culturing of the original data and interpolating the removed (bad) data points using the minimum curvature technique, which is a favourable gridding technique for gridding potential field data due to its smooth surface approximations (Guo et al., 2012; Nabighian et al., 2005). The Reduction to pole techniques was then applied to reduce the effects of deep magnetization and correct for the positions of the magnetic sources responsible for the observed magnetic signatures. The vertical tilt angle was then applied to enhance the edges of both the shallow and deeper magnetic sources in the data, which in turn enhances the lineaments in the data (Miller & Singh, 1994).

Resistivity

The first step in processing the electrical resistivity data was to edit (eliminate) bad points caused by current deficit at large offsets or bad contact with the ground. A regularized (weighted least square function) algorithm with linear filtering was used to invert the measured data using the ResiPy

13652478, 2024, 5, Downloaded from https://onlinelibrary.wiley.com/doi/10.1111/1365-2478.13489 by South African Medical Research, Wiley Online Library on [21/05/2024]. See the Terms and Conditions (https://onlinelibrary.wiley.com/terms-and-conditions) on Wiley Online Library for rules of use; OA articles are governed by the applicable Creative Commons License

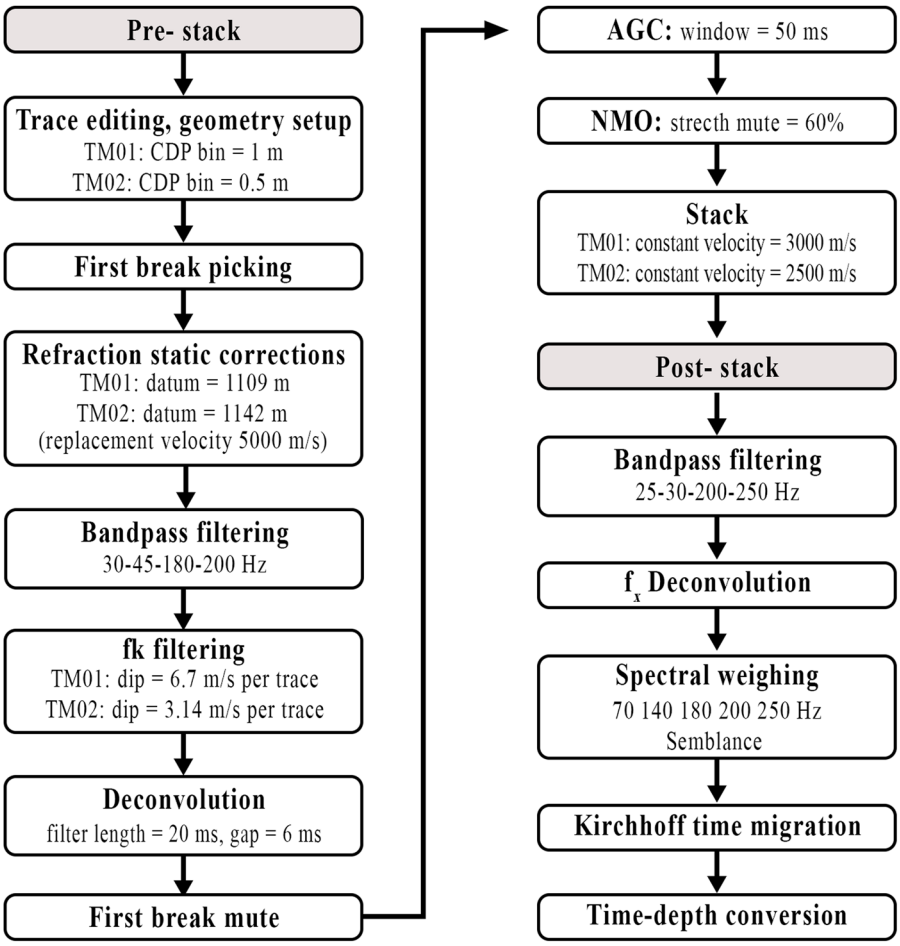

FIGURE 6 Processing flow for the reflection seismic datasets of SP1 and SP2, at Tharisa mine.

package (Blanchy et al., 2020). To account for any complex model geometry, a triangular finite element mesh was constructed prior to the inversion (Binley & Kemna, 2005; Blanchy et al., 2020). The maximum length, electrodes and data points for the resistivity data were 400 m, 123 and 2110, respectively. The final RMS error for each of the three tomograms ranged from 0.9% to 1.3%, whereas the number of iterations varied between the three profiles and arrays. Table 2 shows the data acquisition and processing. In order to estimate not only a total accuracy of the inversion but also that of different parts of the inverted resistivity model, the forward apparent resistivity calculations have been carried out for the inverted models using a finite-difference modelling algorithm. Figure 8a–c shows an example of the measured, calculated and inverted apparent resistivities, respectively, for profile RP1. The topographic effect was not taken into account because the elevation difference was less than 1 m along the profiles.

RESULTS

The P-wave velocity, density, resistivity and magnetic susceptibility measurements showed a narrow range of values within the same samples, with a larger variation observed on P-wave velocities compared to density, resistivity and magnetic susceptibility. Physical properties measurements show that anorthosites (5087.5 m/s) have the lowest P-wave velocities, and norites (5670 m/s) have intermediate values, whereas pyroxenites (5950 m/s) and chromitites (6117.5 m/s) have the highest velocities. We paid more attention to the contrast over the actual velocities and density, as the aim of the physical property measurements was to test if we can seismically distinguish the different rock types within the study area. To present the physical property measurements, we used the lithological data and the physical property measurements to recreate downhole-logging results (Figure 9). To better understand the seismic response of the different rock units, we

13652478, 2024, 5, Downloaded from https://onlinelibrary.wiley.com/doi/10.1111/1365-2478.13489 by South African Medical Research, Wiley Online Library on [21/05/2024]. See the Terms and Conditions (https://onlinelibrary.wiley.com/terms-and-conditions) on Wiley Online Library for rules of use; OA articles are governed by the applicable Creative Commons License

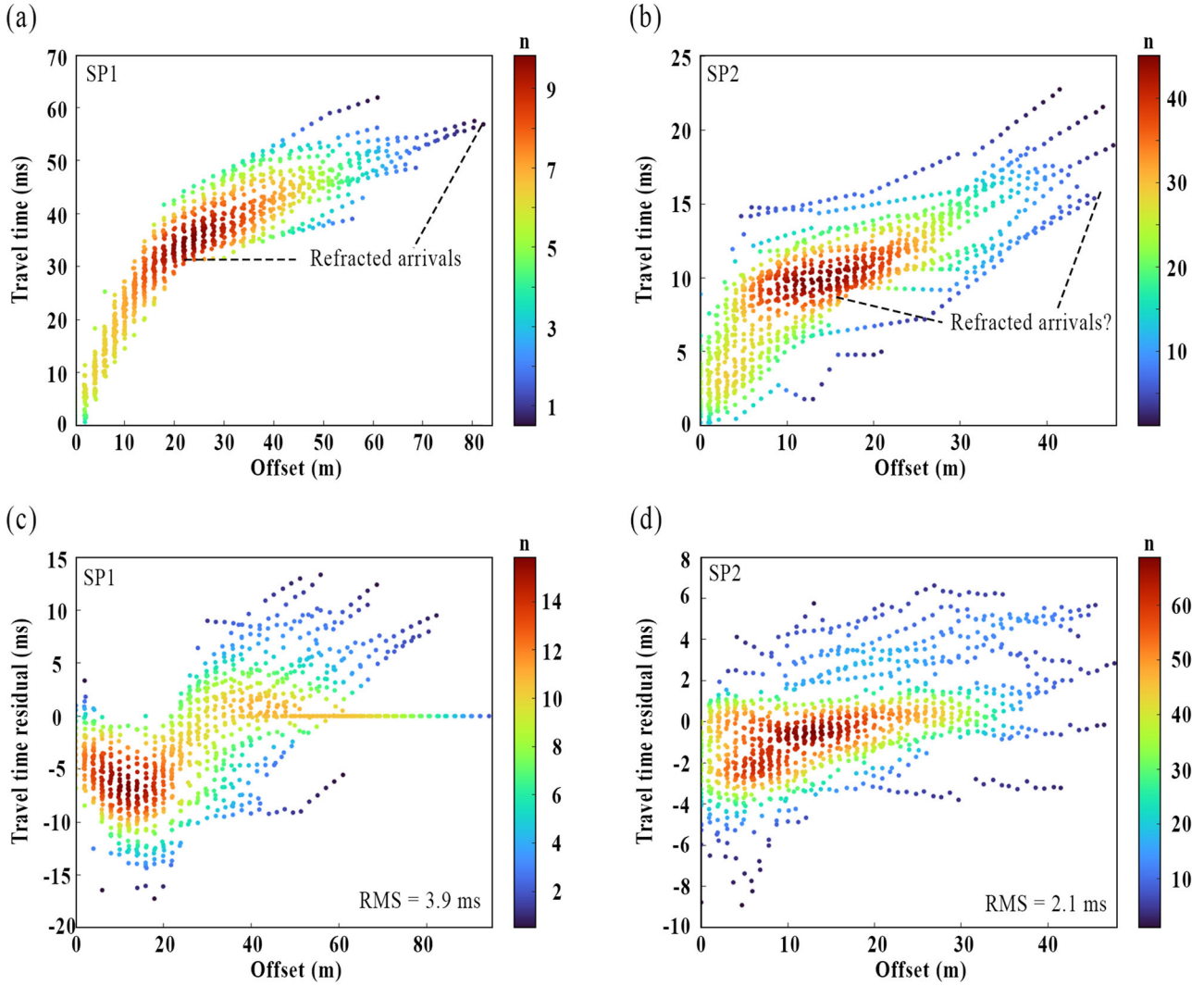

FIGURE 7 Quality check of the first breaks and the inverted tomographic models. (a and b) Example of the first break picks for travel time tomogram as a function of offset for SP1 and SP2, respectively. (c and d) Travel time residuals as a function of offset for the same lines after the last iteration of the tomogram, with an RMS value of 3.9 and 2.1 ms obtained for the profiles. n, number of points within a range.

TABLE 2 Resistivity acquisition and processing parameters.

Profiles	**RP1**	**RP2**	**RP3**
Acquisition			
Array type	Schlumberger, dipole–dipole, Wenner array		
Acquisition system	ABEM Terrameter SAS 1000		
No. of electrodes	41	41	81
Electrode spacing (m)	2	2	6
Strike	E–W	S-N	SE-NW
Profile length (m)	80	80	240
Inversion			
Inversion method	Weighted least square function (regularized inversion with linear filtering)		
Iterations	Schlumberger: 4	Schlumberger: 3	Schlumberger: 2
	Dipole–dipole: 7	Dipole–dipole: 3	Dipole–dipole: 1
RMS	Schlumberger: 0.92	Schlumberger: 0.97	Schlumberger: 1.2
	Dipole–dipole: 1.07	Dipole–dipole: 1.25	Dipole–dipole: 1.0.3

Abbreviation: RMS, root mean square.

13652478, 2024, 5, Downloaded from https://onlinelibrary.wiley.com/doi/10.1111/1365-2478.13489 by South African Medical Research, Wiley Online Library on [21/05/2024]. See the Terms and Conditions (https://onlinelibrary.wiley.com/terms-and-conditions) on Wiley Online Library for rules of use; OA articles are governed by the applicable Creative Commons License

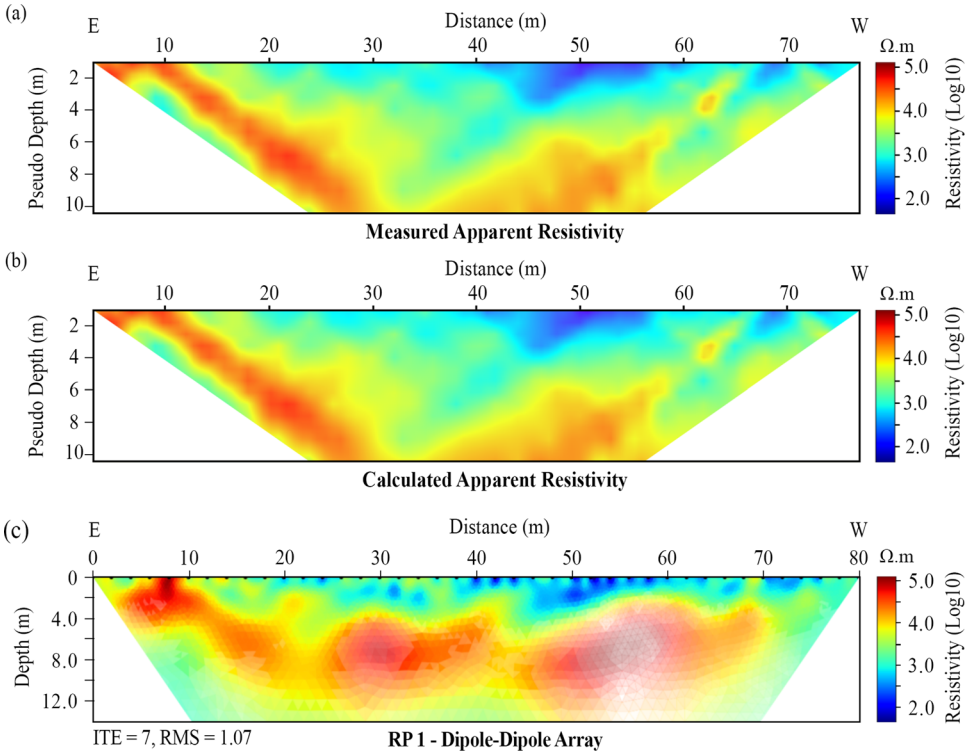

FIGURE 8 (a) Measured and (b) calculated apparent resistivity pseudo sections of profile RP1 using a dipole-dipole array. (c) The inverted resistivity 2D model using a regularized (weighted least square function) inversion after seven iterations (root mean square = 1.07%).

conducted 1D-synthetic seismogram using a MATLAB script (Westgate, 2020) by calculating the reflection coefficient and convolving it with a 130 Hz Ricker wavelet. Pyroxenites show the highest magnetic susceptibility (0.014224524 SI) and the lowest density (2744.5 kg/m^3) (Figure 9). They are known to contain >20% magnesium oxide as reported by (Sepato, 2015). Although the resistivity measurements of pyroxenites are not available, it is expected to have high resistivity, due to the presence of oxide minerals (Parkhomenko, 1982).

Reflection seismic processing focused on cleaning the top 100 ms from ambient and coherent noise in order to enhance target reflections. Although the data were collected in a noisy mine environment, good quality first breaks are observed in all the profiles. Examples of shot gathers from SP1 and SP2 are shown in Figure 5. Note the different noise levels in the profiles. The first profile (SP1) shows evidence of coherent noise (green arrows) on the far offset from drilling. Due to these noise levels in the shot gathers, a significant amount of time was spent on reflection processing with different approaches. The shot gather showed reflections, although it was not convincing. Figure 7 shows the first breaks that were used in the tomography for the profiles in the study area. The plots (Figure 7a,b) show the presence of refracted arrivals on all the seismic profiles, with a root mean square (RMS) between 2 and 4 ms. Given that the seismic data were collected in a noisy area of the mine, the RMS is quite good. Comparing the raw shot gathers and processed shot gathers (Figure 5), the observed noise in the raw gathers has been attenuated, and the reflections have been enhanced. A series of reflections are observed in the processed shot gathers at ~55 and 100 ms for SP1. Figure 10a,b shows 2D velocity models of SP1 and SP2. Note that the seismic tomograms show the presence of three distinct P-wave velocity zones across the two seismic profiles. The near surface P-wave velocities (dark blue zone) exhibit velocities between ~500 and 1300 m/s at varying depths of ~0–8 m across the profiles. The dark blue zone is underlain by a thin light blue P-wave velocity zone of relatively higher velocities ($\sim 1300 - 2100$ m/s). The thickness of this zone varies across the profiles. The third P-wave velocity zone (light yellow to brown) is characterized by velocities between ~ 2100 and 6500 m/s, with variable depth from surface. The velocity zone consists of abrupt low velocity depression within it, possibly caused by fracturing (Figure 10b: white arrows). However, this is inconclusive as we observe poor ray coverage on SP2. We observe a maximum ray penetration of 20–25 m in the velocity models, due to maximum offsets of 98 m. The length of the second profile (SP2) was approximately half the length of the first profile (SP1); thus, the depth of penetration for SP2 is lower (~16 m).

The total magnetic intensity (TMI) map of the study area is presented in Figure 11a,c. Magnetic data processing focused on enhancing linear features within the open pit. Figure 10b,d is the vertical tilt angles. Features on the TMI are pronounced after the removal of the regional magnetic field and reduc-

13652478, 2024, 5, Downloaded from https://onlinelibrary.wiley.com/doi/10.1111/1365-2478.13489 by South African Medical Research, Wiley Online Library on [21/05/2024]. See the Terms and Conditions (https://onlinelibrary.wiley.com/terms-and-conditions) on Wiley Online Library for rules of use; OA articles are governed by the applicable Creative Commons License

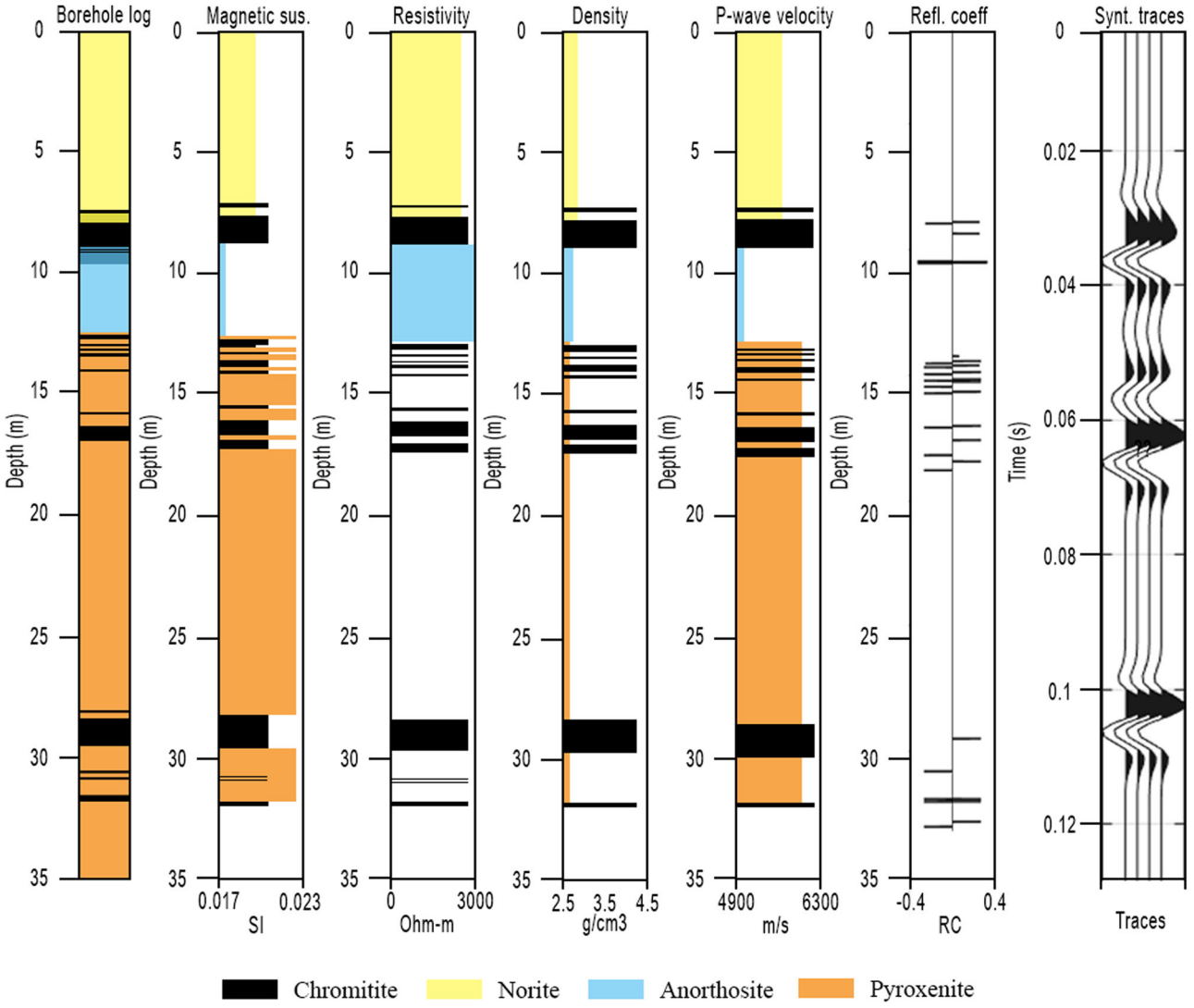

FIGURE 9 Downhole logging and core-logging data that was reconstructed from borehole 1 (BH1) of Tharisa mine. The data show the contact between the mineralization and the host rock (norites, anorthosites and pyroxenites). Chromitites show a significant density and velocity contrast, making them recognizable from the host rocks. The resistivity log shows less variations in resistivity values across the rocks, with no resistivity data available for pyroxenites. Reflection coefficients were convolved with a 130 Hz Ricker wavelet to generate a synthetic seismogram. The colours used for the rock types are consistent throughout the paper.

tion to pole. The pattern of magnetic anomalies indicates the geological structures of the study area. The positive magnetic anomaly (Figure 11b: black arrow) is trending east–west on the southern section of G1. This anomaly is correlated with the dyke (Figure 4b) that crosses the open pit. The negative magnetic anomalies (Figure 11b: blue arrows) are attributed to fracture zones, where a reduction in magnetic susceptibility of the rocks occurs due to the reduction in magnetite grains and alteration of magnetite into hematite (a mineral with less magnetic susceptibility) by water occurs (Harding et al., 1988; Lapointe et al., 1986). The vertical tilt angle was applied to enhance linear features observed on the TMI. The edges of the strong positive magnetic anomaly, due to the mapped dyke, are enhanced together with the negative magnetic signatures that are linked to fracturing. The same process was applied to G2 and G3, with the negative magnetic signatures (Figure 11d: blue arrows) enhanced and attributed to fracturing. The positive magnetic signature (Figure 12) continues into G3 and follows the trend of the mapped dyke.

Inversion of the electrical resistivity data provided us with possible resistivity models. Complex lateral and vertical variations of resistivities are observed on the resistivity models. The Schlumberger (Figure 13) and dipole–dipole (Figure 14) models are considered for this study due to their sensitivity to horizontal (high resistivity zones: white arrows) and vertical (low resistivity: blue arrows) changes in resistivity respectively. RP1 and RP2 were collected inside the pit, with the top layer of the ground dominated by highly fractured rock

13652478, 2024, 5, Downloaded from https://onlinelibrary.wiley.com/doi/10.1111/1365-2478.13489 by South African Medical Research, Wiley Online Library on [21/05/2024]. See the Terms and Conditions (https://onlinelibrary.wiley.com/terms-and-conditions) on Wiley Online Library for rules of use; OA articles are governed by the applicable Creative Commons License

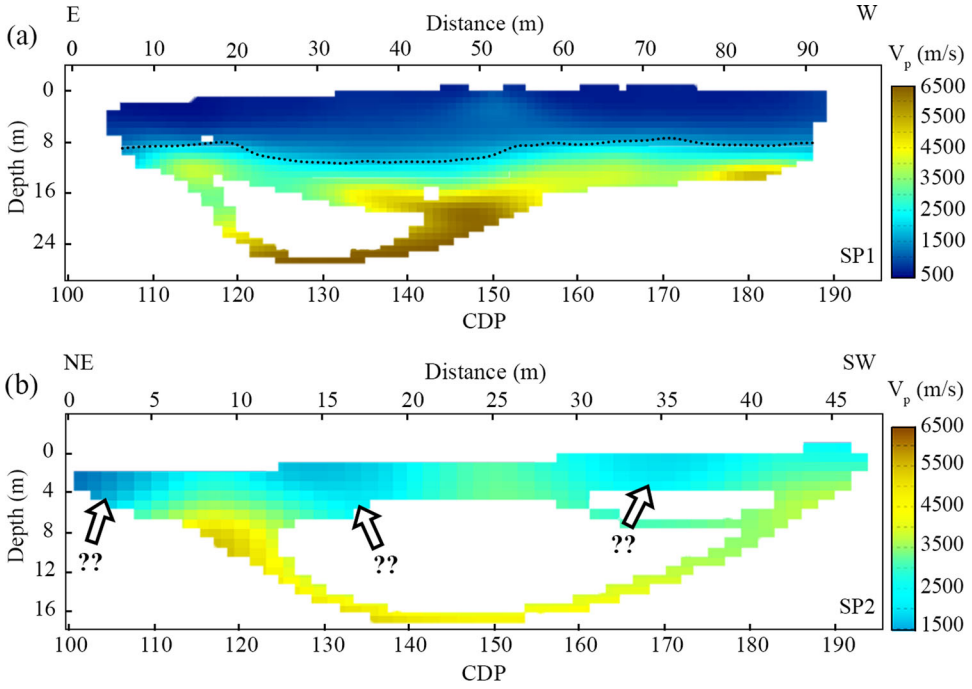

FIGURE 10 2D travel time tomography results, with low velocity depressions marked with white arrows: (a) seismic profile SP1 and (b) profile SP2. Results show ray coverage of approximately 25 m depth.

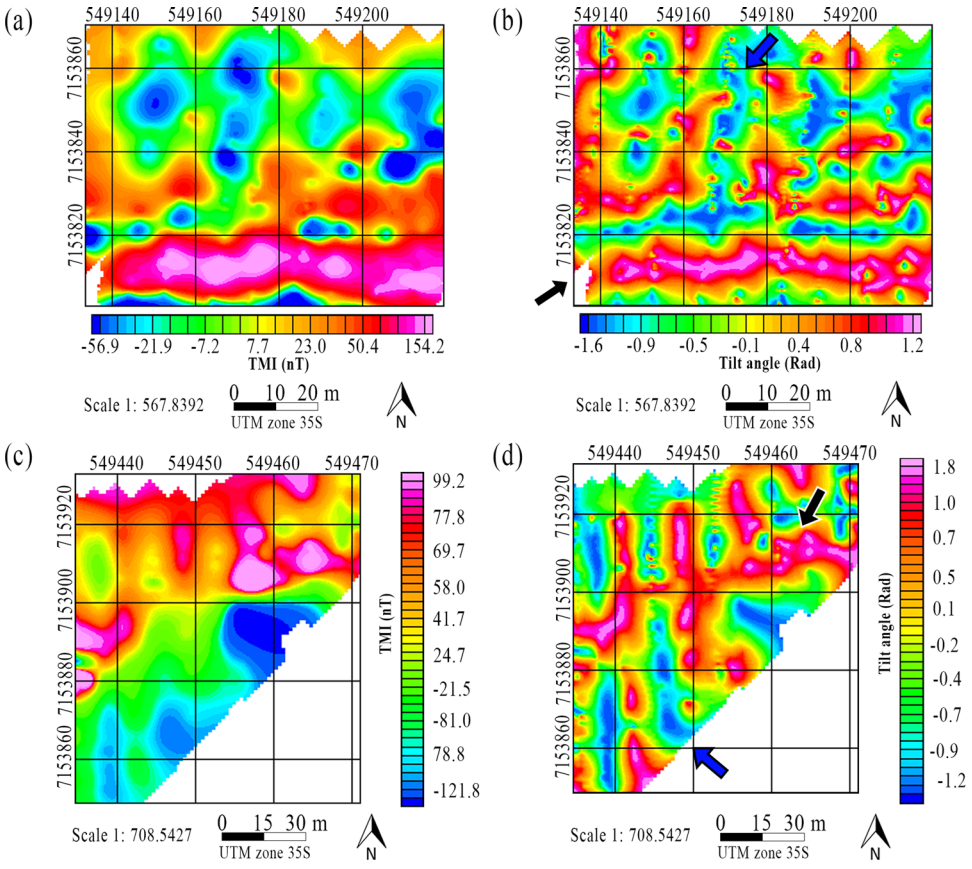

FIGURE 11 (a and c) Total magnetic intensity (TMI) map of Tharisa mine after de-culturing, micro-levelling, and residual de-trending. (b and d) Vertical tilt angle derivative of the TMI maps. The black and blue arrows highlight zones of magnetic highs and lows, respectively.

13652478, 2024, 5, Downloaded from https://onlinelibrary.wiley.com/doi/10.1111/1365-2478.13489 by South African Medical Research, Wiley Online Library on [21/05/2024]. See the Terms and Conditions (https://onlinelibrary.wiley.com/terms-and-conditions) on Wiley Online Library for rules of use; OA articles are governed by the applicable Creative Commons License

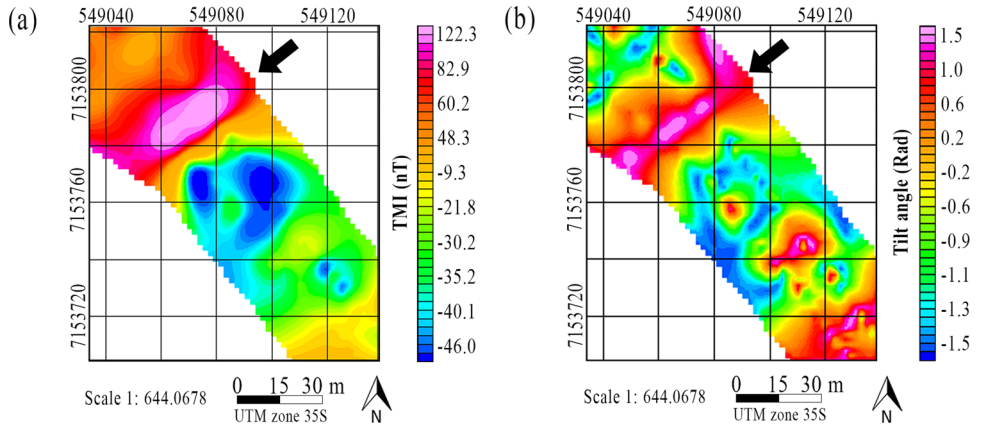

FIGURE 12 (a) Total magnetic intensity (TMI) map of Tharisa mine after de-culturing, micro-levelling, and residual de-trending. (b) Vertical tilt angle derivative of the TMI maps. The black arrows highlight zones of magnetic highs.

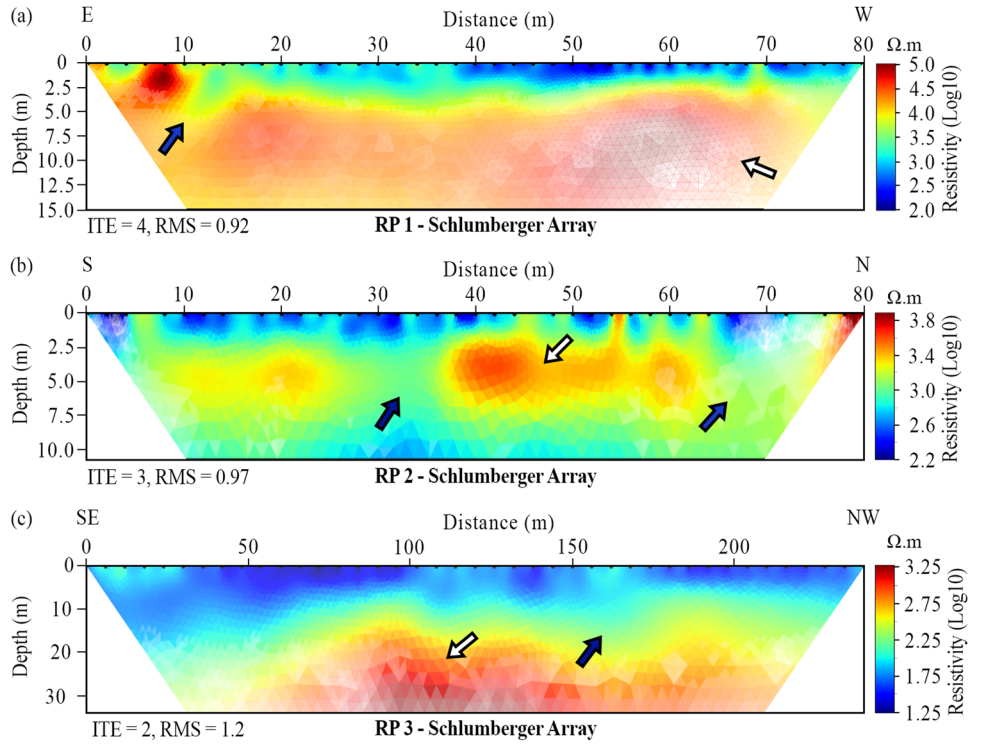

FIGURE 13 Schlumberger electrical resistivity inverse sections for profile (a) RP1, (b) RP2 and (c) RP3. The white arrows indicate areas with high resistivity, while the blue indicates low resistivity areas.

(Figure 15a), then followed by fractured bedrock (Figure 15b). This is visible on the resistivity model as a low resistivity zone (blue zone: ~89 to ~213 Ω/m), followed by an intermediate resistivity zone (light green to yellow: ~213 to ~3274 Ω/m). The intermediate resistivity zone is underlain by a zone of much higher resistivities (~3274 to ~20,000 Ω/m), coloured as light orange to red zone (Figure 15c: Fresh bedrock). RP3 has the greatest highly conductive layer that has thicknesses ranging between 8 and 20 m towards south-eastern side of the profile. These are attributed to the loose sandy-clay soil (Figure 15d) that is close to the river. The Schlumberger models show conductive layers (low resistivity and blue coloured zone) thickness between 2.5 and 14 m across the profiles.

INTERPRETATIONS

Figure 16 compares and correlates the resistivity models, seismic tomograms and seismic reflection data across SP1 and RP1, together with the lithological data from borehole

13652478, 2024, 5, Downloaded from https://onlinelibrary.wiley.com/doi/10.1111/1365-2478.13489 by South African Medical Research, Wiley Online Library on [21/05/2024]. See the Terms and Conditions (https://onlinelibrary.wiley.com/terms-and-conditions) on Wiley Online Library for rules of use; OA articles are governed by the applicable Creative Commons License

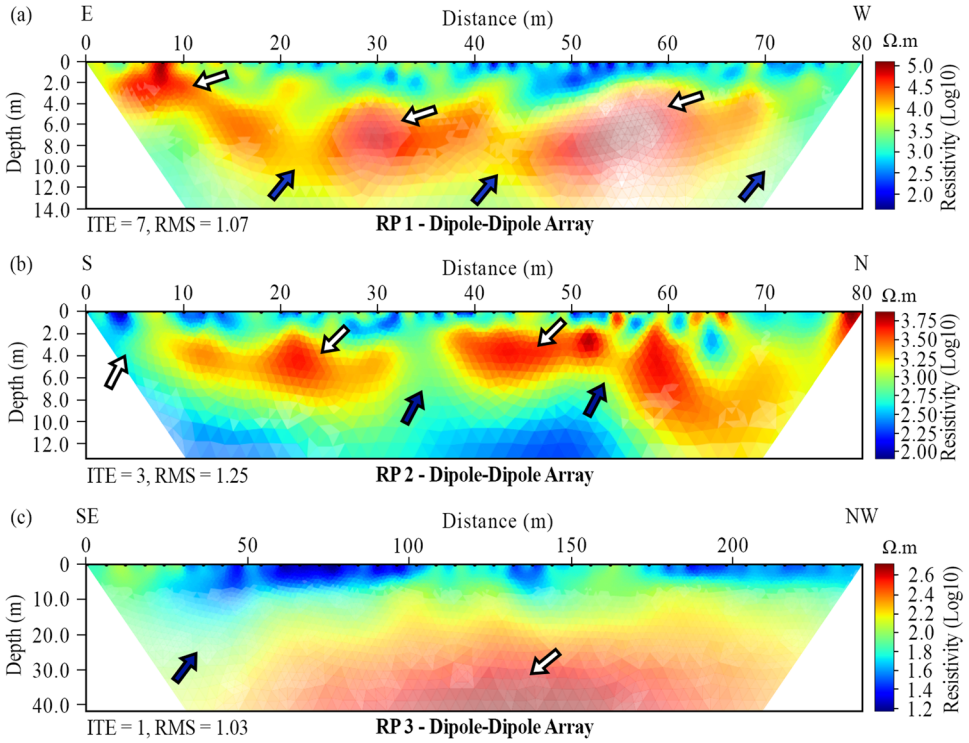

FIGURE 14 Dipole–dipole electrical resistivity inverse sections for profile (a) RP1, (b) RP2 and (c) RP3. The white arrows indicate areas with high resistivity, whereas the blue indicates low resistivity areas.

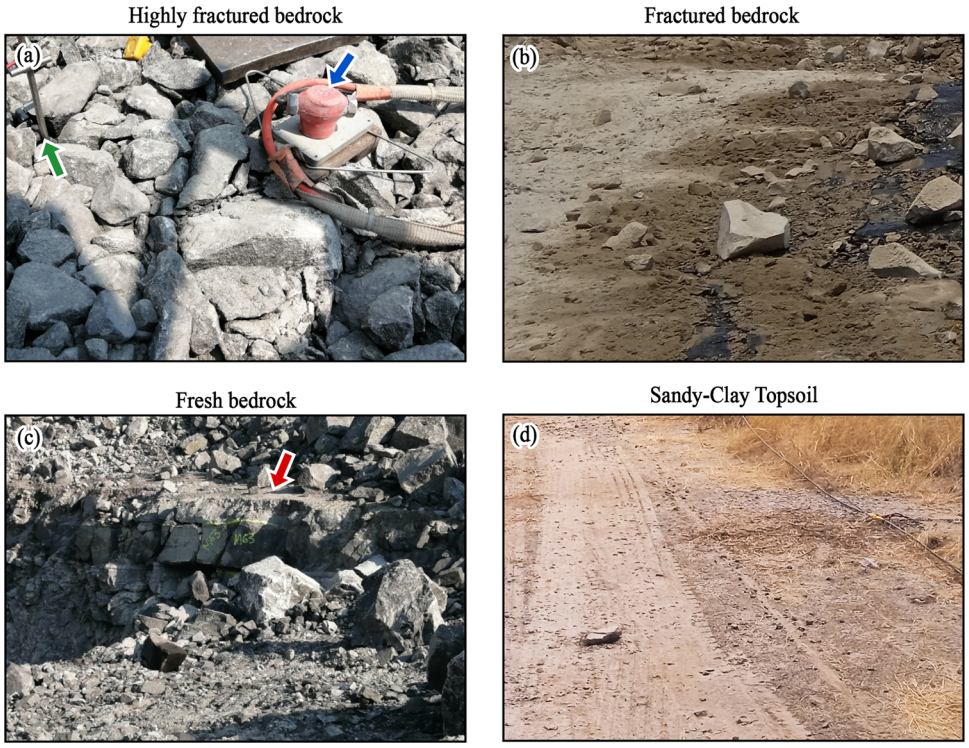

FIGURE 15 Field ground conditions. Resistivity and seismic profiles were collected in an active mine. Diagrams show (a) highly fracture rock, (b) fractured rock and (c) fresh bed rock (red arrow) inside an open pit. (d) Sandy-clay weathered topsoil outside the pit. Green arrow indicates the resistivity electrodes, whereas the blue arrows show the land streamer used to collect seismic data.

13652478, 2024, 5, Downloaded from https://onlinelibrary.wiley.com/doi/10.1111/1365-2478.13489 by South African Medical Research, Wiley Online Library on [21/05/2024]. See the Terms and Conditions (https://onlinelibrary.wiley.com/terms-and-conditions) on Wiley Online Library for rules of use; OA articles are governed by the applicable Creative Commons License

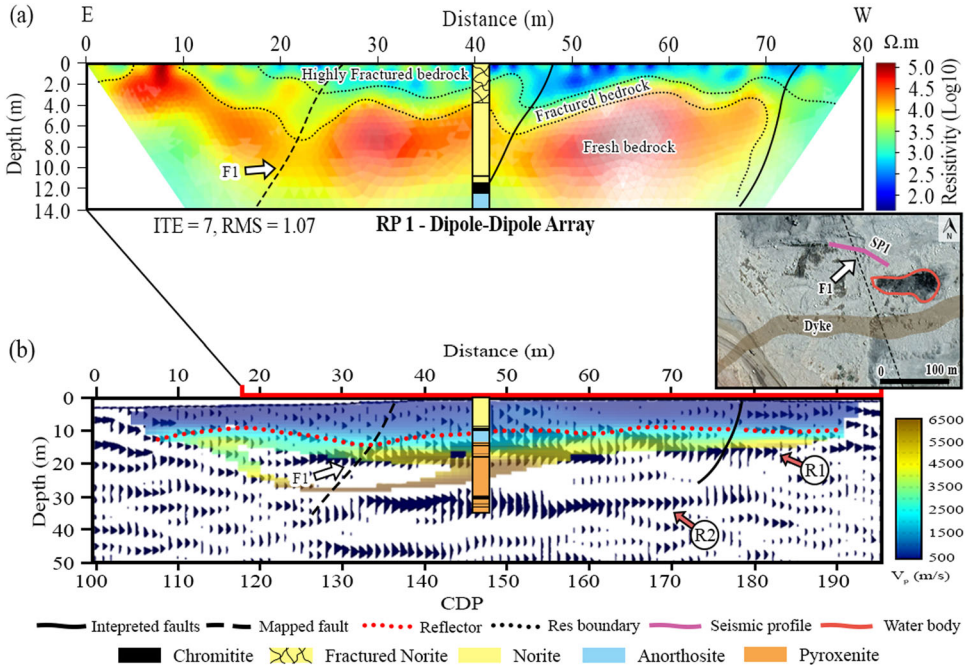

FIGURE 16 Integrated and interpreted results of resistivity and seismic refraction and reflection stack. (a) Resistivity tomogram (RP1). (b) Seismic tomogram overlaid on migrated depth stack section for input seismic profile (SP1). The dotted lines show the lithological boundaries between the top weathered rock and fresh bedrock. The solid black lines represent the interpreted joints and fractures. Insert shows the location of the resistivity and the seismic profile with the cross-cutting fault pointed with a white arrow.

1 (Figure 4). Both the resistivity model and seismic velocity model results correlate with the borehole (BH1) data. The top 6 m on the borehole (Figure 16a,b) corresponds with the light blue and dark blue zones that represent the low resistivity and seismic velocity zones, respectively. The dark blue to light green zones on the resistivity model is characterized by resistivities of $\leq 89-213\ \Omega/\mathrm{m}$ and P-wave velocities of $\leq 500-1300$ m/s. This zone is interpreted to be the top highly fractured norites, due to blasting in the pit. An increase in resistivity and P-wave velocity of the subsurface rocks is observed with increasing depth. The transition between the highly fractured and fresh bedrock at depths of 6–8 m is characterized by the higher resistivities and P-wave velocities of $213-3274\ \Omega/\mathrm{m}$ and $1300-2100$ m/s. The layers situated beneath the transition zone, starting with the fresh norite at depths of about 8 m and extending to greater depths, are characterized by higher resistivities of $\sim 3274-20,000\ \Omega/\mathrm{m}$ and P-wave velocities of $\sim 2100-6500$ m/s. These layer is interpreted to be the fresh bedrock made up of the norite, anorthosite and chromitite rocks that have not been affected by blasting (Figure 16a,b). The electrical resistivity and seismic velocity models show inhomogeneous horizons, with sudden resistivity changes that are attributed to fractures. However, the P-wave velocity model (Figure 10a) shows less lateral velocity changes; therefore, no interpretation of lateral P-wave velocity changes can be made. The dipole–dipole resistivity and seismic reflection sections reveal that the lithology within the pit is disturbed. The inversion model (Figure 17a) shows a depression at the centre of the profile which can be attributed to the highly fractured bedrock. However, the interpretation of the fracture systems along the bench of the pit is inconclusive as the ray coverage on SP2 is poor. The seismic profiles need to be expanded and improve the ray penetration and coverage before any interpretation can be made. A series of reflections (Figure 17b) observed in SP2 are interpreted to be contacts between highly fractured, fractured bedrock and fresh bedrock.

Reflection seismics was mainly used to image the deeper discontinuities and the mineralization contacts. On SP1, a near surface reflection is observed (Figure 16b). The reflection (R1) is generally flat throughout the seismic profile and can be correlated with the subsurface mineral contact between the chromitites and its host rock at depth (Figure 16b). The origins of the reflections are further confirmed by the sidewall mapping (shown in Figure 1d) of the chromitite layers. The continuity of the reflection is disturbed at 30–40 m on the migrated stack section, and this correlates with the resistivity discontinuity observed in Figure 16a (dashed line). This discontinuity is associated with the mapped fault (F1) within the pit (shown on insert of Figure 16). A similar package of reflections (R2) are observed at 30 m depth, and this can be attributed to the lower mineralization (MG2); however, the

13652478, 2024, 5, Downloaded from https://onlinelibrary.wiley.com/doi/10.1111/1365-2478.13489 by South African Medical Research, Wiley Online Library on [21/05/2024]. See the Terms and Conditions (https://onlinelibrary.wiley.com/terms-and-conditions) on Wiley Online Library for rules of use; OA articles are governed by the applicable Creative Commons License

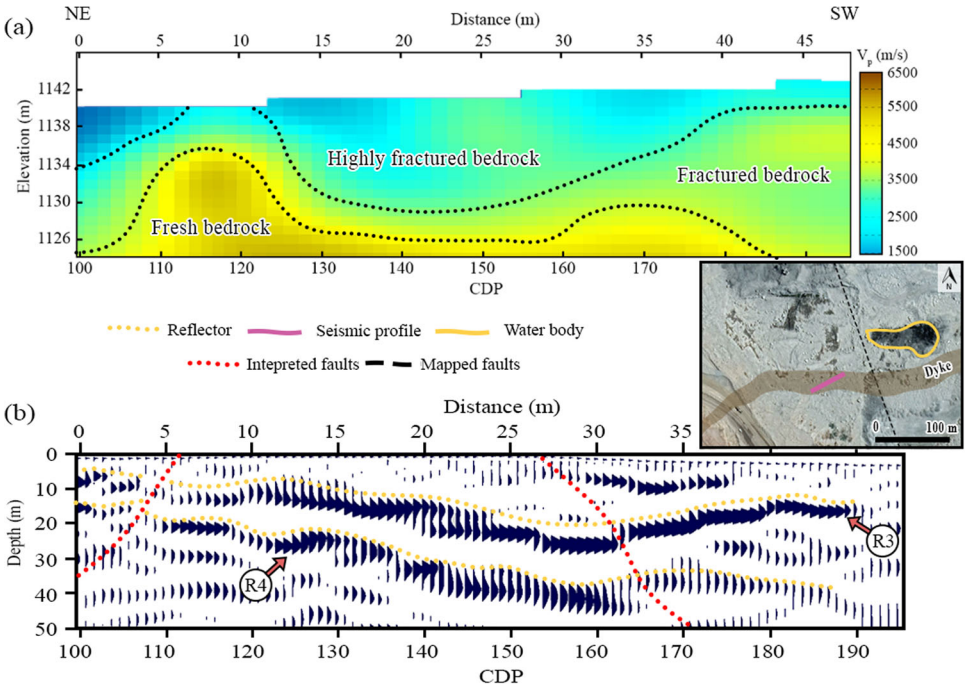

FIGURE 17 (a) Tomography results and (b) migrated depth reflection section of SP2 showing reflections dipping to the south west, interpreted as a series of anorthosites and norite succession (grey arrows), that are markers for chromitite mineralization. Low-velocity zones are indicated with red arrows and correspond with interpreted faults on the stack section. Insert shows the location of the seismic profile with the cross-cutting dyke (brown) and fault (black dashed line).

interpretation of this is inconclusive as there is no borehole information that can constrain the depth of the MG2 mineralization. The two identified reflections are not clear at the edges of the seismic sections and exhibit multiple discontinuities, due to low fold coverage. SP2 was conducted perpendicular to RP2, with the first section of the resistivity profile covering the dyke, whereas the seismic profile is entirely within the dyke. The dyke is covered by highly fractured rock from the mine workings. This is evident on SP2, as it shows low velocity regions towards the south-western side of the profile at varying depths (Figure 17a). The migrated depth sections (Figure 17b) show continuous reflections (R3) that can be followed to the surface towards the north-eastern side of the profile. The top reflection (R3: starting from ~8 m in the north east to ~25 m in the south west) is associated with the contact between the highly fractured and the weathered dyke, the following reflection (R4: starting from ~15 m in the east to ~40 m in the west) is associated with the contact between the weathered dyke zone and a fresh rock dyke. The low velocity depression (Figure 17a) at the centre of the profile corresponds to the syncline nature of the reflections in Figure 17b between 10 and 40 m. Resistivity values over the dyke range from 3000 to >10,000 Ω/m. Significant differential weathering of the host rock is observed at the contacts with the host rock. Such areas are potential for hosting ground water and, therefore, exhibit low resistivity zones (Figure 14b: beginning of the profile and between 30 and 40 m). The tomographic results are presented in a series of 3D views (Figures 18 and 19) to present them in their real location, together with other geophysical data (resistivity and magnetics) and geological data from the mine. Figure 18b shows the low P-wave velocity depression together with the faults (white lines) that were interpreted from regional aeromagnetic data (Figure 4c). The low depressions are thick on the far ends of the profiles and correlate with the projected faults. Further interpretation of the tomography velocity zones resulted in an addition of more fault planes (Figure 18c) that can be associated with fracture systems (Figure 1c) that are mapped in the pit. The interpreted fracture system is evident on the magnetic data (Figure 18d) as low magnetic depressions and correlates well. A high magnetic signature (Figure 19a) is observed on the southern part of the magnetic data and the seismic profiles. The signature is in relation to the dolerite dyke that intruded through the centre of the pit (Figure 19b). The low magnetic regions are correlated with weathered host rock at the contacts.

DISCUSSION

The geophysical data collected at Tharisa mine illustrate that good-quality geophysical dataset can be used to establish

13652478, 2024, 5, Downloaded from https://onlinelibrary.wiley.com/doi/10.1111/1365-2478.13489 by South African Medical Research, Wiley Online Library on [21/05/2024]. See the Terms and Conditions (https://onlinelibrary.wiley.com/terms-and-conditions) on Wiley Online Library for rules of use; OA articles are governed by the applicable Creative Commons License

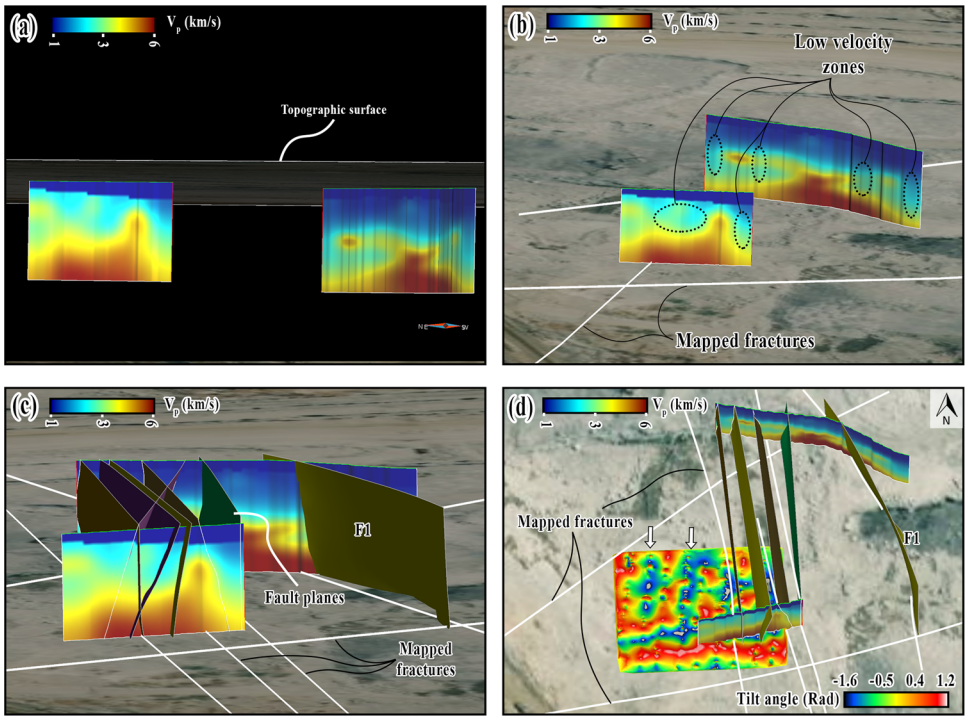

FIGURE 18 A series of 3D views showing seismic tomography results with the location of the seismic lines, interpreted major faults from (Figure 3a) aeromagnetic data. (a) Position of seismic profiles, relative to the open pit, (b) tomographic results, with low-velocity zones indicated along SP1 and SP2, (c) shows the relationship between the interpreted low-velocity zones with the fault structures that where mapped within the pit, (d) top view: relationship between the tilt angle derivative magnetic map and the interpreted fault structures. White arrows indicate areas of low magnetics. White line indicated mapped faults within the pit.

regional structural fracture system in an area of interest. This is likely the first multi-geophysical study to be conducted in an open-pit for imaging fractures in the Bushveld Complex. The data were collected without any interruption to mining activity, illustrating the cost and time effectiveness. The most notable reflection, low magnetic and low resistivity zones originate from the fractures within the open pit. This reflection, magnetic and resistivity zone suggests multiple factors that contributed to the fracture system: (1) Geologically induced fractures that were reactivated during the intrusion of dykes; (2) induced fractures due to mine blasting. The fracture systems could act as conduits for water from the water table and the river. A good correlation among magnetics, P-wave velocity models, resistivity section and seismic data is evident when overlaying the different datasets (Figures 16 and 17). For example, the low magnetic regions correlate with low P-wave velocity or low resistivity zones. This implies that the areas with low magnetics are highly weathered and prone to fracturing. This is supported by the identification of the dyke contact with the host rock exhibiting a low magnetic and resistivity values (Figure 19b). The use of multiple geophysical methods was useful in the interpretation and imaging of structures within a few meters, demonstrating the potential for high resolution geophysical methods in mine noisy environment. The quality of the data is attributed to proper survey design, acquisition and processing. This opens up opportunities for the application of multiple geophysical methods in exploration and mine development. Longer and wider seismic and magnetic grids are likely the best approach to this type of geology and challenges. However, this will be challenging as a result of the active mining and infrastructures.

CONCLUSION

This study has demonstrated that multi-geophysical methods can be utilized to delineate fractures and faults in an active open-pit mine. The combination of three or more geophysical methods has more advantage in subsurface imaging. The geophysical data were complemented by borehole data and physical property measurements of rock samples. The use of geophysical data in a noisy mining environment proved to be challenging; however, seismic data showed good quality first arrivals and refracted arrivals, and this allowed the imaging of the mineralization and host rock along the profiles. Furthermore, the P-wave velocity tomogram provided information about the near surface rock conditions with the highly fractured rock showing as depression zones. Ground

13652478, 2024, 5, Downloaded from https://onlinelibrary.wiley.com/doi/10.1111/1365-2478.13489 by South African Medical Research, Wiley Online Library on [21/05/2024]. See the Terms and Conditions (https://onlinelibrary.wiley.com/terms-and-conditions) on Wiley Online Library for rules of use; OA articles are governed by the applicable Creative Commons License

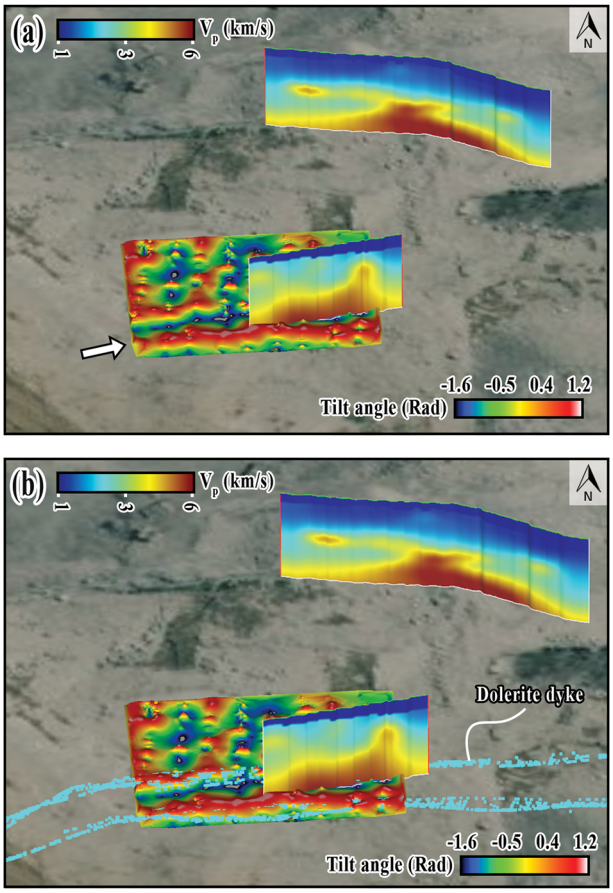

FIGURE 19 (a) 3D views showing seismic tomography results with the location of the seismic lines, tilt angle derivative magnetic map. (b) Relationship between the tilt angle derivative magnetic map and the mapped dyke (Figure 1b).

magnetic data provided high-resolution delineation of a major dyke that was previously identified through aeromagnetic data and geological mapping. Ground magnetic further showed that the dyke is crosscut by a series of fractures and faults that may be potential conduits for water migration into the pit. Electrical resistivity tomography identified linear low resistivity zones that differentiate the fractured and undisturbed hard rock. These results will be integrated with hydrological and geochemical studies to further unravel and determine the source of water that migrates into the pit.

ACKNOWLEDGEMENTS

The support of the Department of Science and Innovation through its funding agency, the National Research Foundation and the Centre of Excellence for Integrated Mineral and Energy Resource Analysis (DSI-NRF CIMERA) towards this research is hereby acknowledged. Opinions expressed and conclusions arrived at are those of the author(s) and are not necessarily to be attributed to the CoE, DSI or NRF. We thank Tharisa Mine for providing access to the site to conduct the geophysical surveys and granting permission to publish the work. We thank several PhD and MSc students from the University of the Witwatersrand, Johannesburg, who took part in the data acquisition stage. We also thank Engineering & Exploration Geophysical Services CC for supporting us with the geophysical equipment, and Schlumberger for the continued support with the licences for Petrel. HiSeis Pty Ltd. and Petrosys are highly appreciated for sponsoring the licenses for Globe Claritas processing software.

DATA AVAILABILITY STATEMENT

The data presented in this study are available upon request from the corresponding authors. The data are not publicly available due to privacy restrictions. Petro-physical data can be found on the website of The Council of Geoscience South Africa (https://maps.geoscience.org.za/portal/apps/sites/#/council-for-geoscience-interactive-web-map-1).

ORCID

Moyagabo K. Rapetsoa https://orcid.org/0000-0003-3275-8994
Musa S. D. Manzi https://orcid.org/0000-0002-1654-5211
Ian James https://orcid.org/0000-0002-1655-3529
Mpofana Sihoyiya https://orcid.org/0000-0003-1956-5223

REFERENCES

Amoush, H.A. & Mashagbeh, A. (2009) Using geophysical methods to image near-surface cylindrical pipeline: a case study on engineering applications, Jordan. *Jordan Journal of Civil Engineering*, 3(2), 13. https://core.ac.uk/download/pdf/234698299.pdf

Basson, I.J. (2019) Cumulative deformation and original geometry of the Bushveld Complex. *Tectonophysics*, 750, 177–202. https://doi.org/10.1016/j.tecto.2018.11.004

Binley, A. & Kemna, A. (2005) DC resistivity and induced polarization methods. In: Rubin, Y. & Hubbard, S. (Eds.) *Hydrogeophysics*, vol. 50: Springer, pp. 129–156. https://doi.org/10.1007/1-4020-3102-5_5

Blanchy, G., Saneiyan, S., Boyd, J., McLachlan, P. & Binley, A. (2020) ResIPy, an intuitive open source software for complex geoelectrical inversion/modeling. *Computers & Geosciences*, 137, 104423. https://doi.org/10.1016/j.cageo.2020.104423

Bumby, A.J., Eriksson, P.G., Catuneanu, O., Nelson, D.R. & Rigby, M.J. (2012) Meso-Archaean and Palaeo-Proterozoic sedimentary sequence stratigraphy of the Kaapvaal Craton. *Marine and Petroleum Geology*, 33(1), 92–116. https://doi.org/10.1016/j.marpetgeo.2011.09.010

Cawthorn, R.G. (2015) The Bushveld Complex, South Africa. In: Charlier, B., Namur, O., Latypov, R. & Tegner, C. (Eds.) *Layered intrusions*. Dordrecht, The Netherlands: Springer, pp. 517–587. https://doi.org/10.1007/978-94-017-9652-1_12

Dahlin, T. (1996) 2D resistivity surveying for environmental and engineering applications. *First Break*, 14(7), 275–283. https://doi.org/10.3997/1365-2397.1996014

Dildar, J., Manzi, M., Abiye, T., Gomo, S., Rapetsoa, M.K. & Drennan, G. (2023) Groundwater Circulation in the Shallow Crystalline Aquifer of Tharisa Mine, South Africa: Evidence fromEnvironmental Isotopes

13652478, 2024, 5, Downloaded from https://onlinelibrary.wiley.com/doi/10.1111/1365-2478.13489 by South African Medical Research, Wiley Online Library on [21/05/2024]. See the Terms and Conditions (https://onlinelibrary.wiley.com/terms-and-conditions) on Wiley Online Library for rules of use; OA articles are governed by the applicable Creative Commons License

and Near-Surface Geophysics. *Water*, 15(16), 2876. https://doi.org/10.3390/w15162876

Eales, H.V. & Cawthorn, R.G. (1996) The Bushveld Complex. In: *Developments in petrology*, vol. 15. Amsterdam: Elsevier, pp. 181–229. https://doi.org/10.1016/S0167-2894(96)80008-X

Gomo, S., Rapetsoa, M.K., Manzi, M.S.D., Onyebueke, E., Dildar, J., Sihoyiya, M. et al. (2023) Integrated geophysical methods for boulder delineation to improve mining. *Geophysical Prospecting*, 71, 1226–1246. https://doi.org/10.1111/1365-2478.13322

Guo, L., Meng, X. & Shi, L. (2012) Gridding aeromagnetic data using inverse interpolation. *Geophysical Journal International*, 189(3), 1353–1360. https://doi.org/10.1111/j.1365-246X.2012.05448.x

Harding, K.L., Morris, W.A., Balch, S.J., Lapointe, P. & Latham, A.G. (1988) A comparison of magnetic character and alteration in three granite drill cores from eastern Canada. *Canadian Journal of Earth Sciences*, 25(8), 1141–1150. https://doi.org/10.1139/e88-112

Hartzenberg, A.G. & Du Plessis, M. (2014) Theinfluence of regional structures associated with the Bushveld Complex on themechanism driving the behaviour of the UG2 hangingwall beam and in-stopepillars at Lonmin's Marikana Operations. *In: The 6th International Platinum Conference. Pretoria: University of Pretoria*. https://repository.up.ac.za/bitstream/handle/2263/71695/Hartzenberg_Structural_2019.pdf?sequence=1

James, I., Hird, G. & Fitzpatrick, A. (2019) Refraction tomography at the Nova Ni-Cu mine. *ASEG Extended Abstracts*, 2019(1), 1–3. https://doi.org/10.1080/22020586.2019.12073152

Kerrigan, N.P. (2013) *Using shallow geophysical methods to locate a buried stream channel at a stream restoration site in the burd run waterhed, Shippensburg, PA*, Shippensburg, PA: Shippensburg University. https://www.ship.edu/globalassets/geo-ess/kerrigan_thesis_131213.pdf

Kinnaird, J.A. (2005) *The Bushveld large igneous province the review paper*, Johannesburg South Africa: The University of the Witwatersrand. http://www.largeigneousprovinces.org/sites/default/files/BushveldLIP.pdf

Lapointe, P., Morris, W.A. & Harding, K.L. (1986) Interpretation of magnetic susceptibility: a new approach to geophysical evaluation of the degree of rock alteration. *Canadian Journal of Earth Sciences*, 23(3), 393–401. https://doi.org/10.1139/e86-041

Lotheringen, J., James, J., Lomberg, K. & Bornman, H. (2016) *Tharisa* chrome *and PGM* mine*, South Africa. Competent* persons report [Competence report No. JTHA011]. Roodepoort: Coffey Mining. https://www.tharisa.com/pdf/investors/annual-reports/2016/cpr-2016.pdf

Malehmir, A., Andersson, M., Lebedev, M., Urosevic, M. & Mikhaltsevitch, V. (2013) Experimental estimation of velocities and anisotropy of a series of Swedish crystalline rocks and ores: velocities and anisotropy of a series of crystalline rocks and ores. *Geophysical Prospecting*, 61(1), 153–167. https://doi.org/10.1111/j.1365-2478.2012.01063.x

Manzi, M., Durrheim, R. & Webb, S. (2017) 3D seismic attributes for platinum exploration and mine planning in the Bushveld Complex (South Africa). In: International geophysical conference, Qingdao, China*, 17–20 April 2017*. Qingdao, China: Society of Exploration Geophysicists and Chinese Petroleum Society. pp. 665–668. https://doi.org/10.1190/IGC2017-169

Maré, L.P. (2022) *Council for Geoscience Petrophysical Properties Atlas*. Pretoria: Council for Geosciences. https://maps.geoscience.org.za/download/petrophysics-map-package.php

Maries, G., Malehmir, A. & Marsden, P. (2020) Cross-profile seismic data acquisition, imaging, and modeling of iron-oxide deposits: a case study from Blötberget, south-central Sweden. *Geophysics*, 85(6), B233–B247. https://doi.org/10.1190/geo2020-0173.1

Miller, H.G. & Singh, V. (1994) Potential field tilt—a new concept for location of potential field sources. *Journal of Applied Geophysics*, 32(2), 213–217. https://doi.org/10.1016/0926-9851(94)90022-1

Nabighian, M.N., Grauch, V.J.S., Hansen, R.O., LaFehr, T.R., Li, Y., Peirce, J.W. et al. (2005) The historical development of the magnetic method in exploration. *Geophysics*, 70(6), 33ND–61ND. https://doi.org/10.1190/1.2133784

Ofterdinger, U., MacDonald, A.M., Comte, J.-C. & Young, M.E. (2019) Groundwater in fractured bedrock environments: managing catchment and subsurface resources—an introduction. *Geological Society, London: Special Publications*, 479(1), 1–9. https://doi.org/10.1144/SP479-2018-170

Parkhomenko, E.I. (1982) Electrical resistivity of minerals and rocks at high temperature and pressure. *Reviews of Geophysics*, 20(2), 193. https://doi.org/10.1029/RG020i002p00193

Pazzi, V., Di Filippo, M., Di Nezza, M., Carlà, T., Bardi, F., Marini, F. et al. (2018) Integrated geophysical survey in a sinkhole-prone area: microgravity, electrical resistivity tomographies, and seismic noise measurements to delimit its extension. *Engineering Geology*, 243, 282–293. https://doi.org/10.1016/j.enggeo.2018.07.016

Perritt, S. & Roberts, M. (2007) Flexural-slip structures in the Bushveld Complex, South Africa? *Journal of Structural Geology*, 29(9), 1422–1429. https://doi.org/10.1016/j.jsg.2007.06.008

Rapetsoa, M.K., Manzi, M.S.D., Westgate, M., Sihoyiya, M., James, I., Onyebueke, E. et al. (2022) Cost-effective in-mine seismic experiments to image platinum deposits and associated geological structures at Maseve platinum mine, South Africa. *Near Surface Geophysics*, 20, nsg.12216. https://doi.org/10.1002/nsg.12216

Reynolds, J.M. (2011) *An introduction to applied and environmental geophysics*. New York: John Wiley & Sons. https://www.wiley.com/en-sg/An+Introduction+to+Applied+and+Environmental+Geophysics%2C+2nd+Edition-p-9780471485353

Roberts, M.K.C. & Clark-Mostert, V. (2010) Is there some commonality between the geological structures in the Bushveld Complex and the Great Dyke? In: *The 4th international platinum conference*, Rosebank: The Southern African Institute of Mining and Metallurgy, pp. 149–153 https://www.saimm.co.za/Conferences/Pt2010/149-156_Roberts.pdf

Sepato, O. (2015) *Statistical and wavelet analysis of density and magnetic susceptibility data from the Bushveld Complex, South Africa.* Johannesburg: University of the Witwaterrand. http://hdl.handle.net/10539/18528

Titus, R., Witthüser, K. & Walters, B. (2009) Groundwater and mining in the Bushveld Complex. In: *Proceedings of the International Mine and Water Conference, Extended Abstracts*, pp. 178–294. https://www.imwa.info/docs/imwa_2009/IMWA2009_Titus.pdf

Van Schoor, A.M. (2002) Detection of sinkholes using 2D electrical resistivity imaging. *Journal of Applied Geophysics*, 50(4), 393–399. http://hdl.handle.net/10204/1474

13652478, 2024, 5, Downloaded from https://onlinelibrary.wiley.com/doi/10.1111/1365-2478.13489 by South African Medical Research, Wiley Online Library on [21/05/2024]. See the Terms and Conditions (https://onlinelibrary.wiley.com/terms-and-conditions) on Wiley Online Library for rules of use; OA articles are governed by the applicable Creative Commons License

Westgate, M.C. (2020) *Reappraisal of legacy reflection seismic data using advanced processing techniques and seismic attributes*. Johannesburg: University of the Witwatersrand, South Africa. https://hdl.handle.net/10539/31030

Wilson, A.H. (2005) Rock-strength and physical properties of Norites of the Merensky and Bastard Units, western Bushveld Complex. *South African Journal of Geology*, 108(4), 525–540. https://doi.org/10.2113/108.4.525

Zhang, J. & Toksöz, M.N. (1998) Nonlinear refraction traveltime tomography. *Geophysics*. 63(5), 1726–1737. https://doi.org/10.1190/1.1444468

How to cite this article: Rapetsoa, M.K., Gomo, S., Manzi, M.S.D., James, I., Dildar, J., Durrheim, R.J. et al. (2024) Multi-geophysical methods for characterizing fractures in an open pit mine, western Bushveld Complex, South Africa. *Geophysical Prospecting*, 72, 1950–1970. https://doi.org/10.1111/1365-2478.13489

13652478, 2024, 5, Downloaded from https://onlinelibrary.wiley.com/doi/10.1111/1365-2478.13489 by South African Medical Research, Wiley Online Library on [21/05/2024]. See the Terms and Conditions (https://onlinelibrary.wiley.com/terms-and-conditions) on Wiley Online Library for rules of use; OA articles are governed by the applicable Creative Commons License